Additive Manufacturing 46 (2021) 102138

Contents lists available at ScienceDirect

Additive Manufacturing

journal homepage: www.elsevier.com/locate/addma

Implications for accurate surface temperature monitoring in powder bed fusion: Using multi-wavelength pyrometry to characterize spectral emissivity during processing

Alfonso Fernandez[a,b,*], Ralph Felice[c], César A. Terrazas-Nájera[a,b], Ryan Wicker[a,b,*]

[a] W. M. Keck Center for 3D Innovation, The University of Texas at El Paso, El Paso, TX 79968, USA
[b] Department of Mechanical Engineering, The University of Texas at El Paso, El Paso, TX 79968, USA
[c] FAR Associates, Macedonia, OH 44056, USA

ARTICLE INFO

Keywords:
Multi-wavelength pyrometry
Accurate surface temperatures
Electron beam melting
Radiation thermometry
Solid and liquid metal emissivity

ABSTRACT

Radiation thermometry methods used in powder bed fusion (PBF) additive manufacturing for in situ monitoring and control and quality assurance are increasing in importance. Arguably, the most significant challenge associated with radiation thermometry methods is the limited understanding of the emissivity, that is the emissive behavior of the entire region being measured. This work describes a new approach for measuring the emissive behaviors of PBF materials during processing using a multi-wavelength (MW) or Spectropyrometer operating in the spectral range from 1000 to 1650 nm. The approach was implemented in an electron beam (EB) PBF machine, using the electron beam as a heat source, allowing for (1) measuring spectral emissive behavior of the surface in a fixed small region (~2.65 mm) throughout a variety of dynamic processing conditions including heating, melting, and cooling; (2) controlling the scanning (heating) profile during processing while rejecting radiative interference in the measurements due to heating lasers (~1070 nm) commonly used in laser PBF; and (3) processing in an evacuated environment to assist with reduction of additional environmental effects that could impact the measurements. The experimental setup included a sight tube that prevented both metallization of the viewport and resultant signal decay, which enabled near-continuous measurements throughout processing. Measurements from the MW pyrometer were compared against those of a type K thermocouple that was placed in the vicinity of the measurement area. Prior to the powder bed preheating experiment, the MW pyrometer was calibrated against a NIST traceable blackbody source. The utility of the approach was demonstrated by acquiring measurements from the surface of a copper (d50~75 μm) powder bed that was progressively heated in a series of nine steps inside an Arcam A2 EB-PBF system through scanning with the electron beam. Following the preheat steps, seven consecutive melt steps were implemented enabling measurements of the emissive behavior for copper during its multiple solid-liquid-solid transitions. The unique capabilities of the MW pyrometer provided measured values of emissivity of copper that exhibited temporal, spectral (1080–1640 nm) and thermal dependence, verifying the non-graybody behavior for copper. Ongoing work will demonstrate the applicability of this technique across multiple powder metal alloy systems and PBF technologies.

1. Introduction

In recent years, powder bed fusion (PBF) additive manufacturing (AM) methods have been gaining popularity for use in various applications spanning medicine, aerospace, and defense. PBF, including laser powder bed fusion (L-PBF) and electron beam powder bed fusion (EB-PBF) techniques have progressively seen enhancements in performance through the addition of increased capabilities such as higher power of the heat source (i.e. laser or electron beam), larger processing envelopes, and a growing catalog of materials. Despite this progress, much research is still focused on establishing robust techniques for monitoring that can enable feedback and control, and that can help ensure quality assurance and process repeatability. Of the several process variables that can be monitored during PBF, temperature is arguably the most important as it

---

* Corresponding author at: W. M. Keck Center for 3D Innovation, The University of Texas at El Paso, El Paso, TX 79968, USA.
E-mail addresses: Afernandez16@miners.utep.edu (A. Fernandez), raffar@pyrometry.com (R. Felice), caterrazas2@utep.edu (C.A. Terrazas-Nájera), rwicker@utep.edu (R. Wicker).

https://doi.org/10.1016/j.addma.2021.102138
Received 9 December 2020; Received in revised form 30 April 2021; Accepted 19 June 2021

provides a direct indication of the thermo-mechanical history of a material. The ability to acquire accurate temperature and other thermal signatures from the powder bed can be used for enhancing process control, helping to achieve process repeatability, and leading to quality assurance while producing components using PBF processes.

Radiation thermometry methods including near infrared (NIR) and infrared (IR) imaging and others, have been used extensively to monitor apparent temperature within the EB-PBF process [1–7]. However, the elevated temperature environment, the processing under vacuum (i.e. 2.0^{-3}mBar), and the non-equilibrium solidification conditions, make process monitoring challenging. For example, the elevated vacuum restricts the use of electronic devices that might require shielding through active cooling and pressurization to function inside the processing chamber. The high vacuum also results in vaporization and condensation of light alloying elements (i.e. aluminum) that can occlude non-shielded viewports used for observations. The use of feedthroughs for electrical sensors (thermocouples) is possible; however, the use of thermocouples requires contact with the material under study, which might not be feasible during PBF fabrication due to the layer-by-layer nature of these processes. In PBF, thermocouples are typically placed at a single location within or below the build platform and are not able to directly monitor individual layer temperatures during fabrication.

Responding to these limitations, temperature monitoring of EB-PBF using non-contact methods has been carried out employing externally installed setups with dynamic viewport shielding. For example, the work by Rodriguez et al. described the implementation of IR thermography through a Zinc-Selenide (ZnSe) window protected by a shutter mechanism in an Arcam A2 EB-PBF system [1]. This setup was used to approximate part surface temperatures and enabled operators to perform changes in processing parameters to homogenize temperatures for various parts built in a single setup. Subsequent work with the same experimental setup, along with a custom developed software interface, demonstrated automatic process control to enact parameter changes that influenced temperature and microstructure of the fabricated parts [2]. Other similar works have described near IR thermography to correlate the presence of defects in the deposited layers with areas of high heat radiation [3] or to perform in situ metrology through comparison of geometrical features in each layer with the expected geometries from the original computer aided design (CAD) model [4].

A method using mid-wave IR cameras was presented by Dinwiddie et al. for online monitoring in EB-PBF that included calibration procedures to account for loss in transmittance through the lead glass and Kapton film used to protect the optical path [5]. Their results included mathematical expressions that were used to obtain the surface emissivity of sintered powder and of the as deposited metal for calibration of IR thermographs during monitoring of Ti6Al4V and Inconel 718 builds. Building upon those results, the work by Raplee et al. [6] presented a method to calibrate temperature profiles extracted from thermographic data accounting for the change in emissivity during preheating and melting in EB-PBF. The method was then employed to approximate the thermal gradient and the velocity at the solidification interface and compared with microstructural quantifications of grain size and morphology. Similarly, recent work by Boone et al. presented a method for NIR imaging in EB-PBF using a borescope that permitted continuous imaging of the process. Using this methodology, the authors carried out an emissivity correction for the measured temperatures through direct image segmentation of an area containing approximate melt-pool dimensions unto which constant values of emissivity were assigned depending on whether the material was considered melted or unmelted [7]. However, this study provided no details of the actual emissivity values used nor how the segmentation of the area corresponding to the melted material was performed. Irrespective of the method, as will be shown in more detail in the current work, emissivity of the process is time-dependent (due to the dynamic process), temperature-dependent, and wavelength dependent, among other factors, suggesting that any method that assigns a single value for emissivity to the material (spatially or temporally) will increase uncertainties in the accuracies of the measurements.

In the studies referenced above, the ability of IR sensors to image large sections of the powder bed was highlighted. This is different from other non-contact thermometry devices, that have been deployed in PBF AM, and that are typically used for measuring thermal signatures in a small region, such as most single and two-color pyrometers. For most IR cameras (employing either photon or thermal detectors) and brightness pyrometry systems, the emissivity of the target must be prescribed over the wavelength range of the detector and the value of emissivity is assumed to remain constant throughout observations, when in fact, emissivity behaves dynamically for most materials, as it is influenced by several material and environment factors [8]. The evolving emissivity during the phase changes experienced in PBF AM is a significant challenge that can introduce substantial error in measurements, with temperature discrepancies that can span tens to hundreds of degrees. For example, a 90 K difference was described between corrected and uncorrected temperatures in the study by [7]. The work described in [6] highlighted the effects on accuracy for IR imaging following melting, where thermographs without emissivity correction showed regions that experienced a decrease in temperature after melting anywhere from 50 °C to 100 °C. Finally, a drastic impact resulting from uncorrected emissivity values was described in [1] during monitoring EB-PBF processing of Ti6Al4V, showing variations in measured temperature that could be in excess of 300 °C. As acknowledged by Murphy and Forrest [9], the correction methods, such as those reviewed above, may fall short given that emissivity correction should be dynamic. Irrespective of the method and as will be shown in more detail in the current work, the emissivity of a target (or emitting region being observed by a sensor) is temporally and spectrally dependent. The emissive behavior can change dynamically based on morphology and topography, surface and bulk chemistry, phase, temperature, and also on the measurement conditions such as the spectral range (wavelength of the emission), atmosphere (the environmental conditions through which the radiation is transmitted), and the angle of measurement, to mention a few [10]. This dynamic behavior of emissivity and other properties can only be exacerbated during the non-equilibrium processing conditions experienced in PBF AM leading to uncertainties in the accuracy of non-contact thermal measurements.

In this work, we report on a novel approach, employing a multi-wavelength (MW) pyrometer, to measure thermal signatures including temperature and spectral emissivity values (measured at 15° from the normal of the powder bed) for a small region of a copper powder bed heated in an Arcam A2 EB-PBF system. The approach included a sight tube that prevented metallization of the viewport and enabled near-continuous measurements throughout heating, melting, and cooling experienced during dynamic PBF processing. This represents an advancement over the methods described in our group's prior work in which metallization of the viewport occurred while measuring with the same MW pyrometer in EB-PBF, resulting in degradation of the intensity signals acquired by the device [11,12]. The measurements are not only important and relevant for thermal monitoring in EB-PBF, but the use of EB-PBF represents an important platform for experimentation for the measurement of spectral emissivities of metal powders during thermal processing that, more generally, are processed in L-PBF and in other processes. For the experiment presented here, the preheating of the copper powder bed was performed through direct scanning of the surface with the electron beam. The temperature of the powder bed was elevated and sustained in a total of nine preheating steps by progressively increasing the electrical current delivered to the beam (in increments of 5 mA). After preheating, seven successive melting steps were also carried out in an area enclosing the small region (target) observed by the pyrometer, enabling the capture of the thermal signatures during phase transitions from powder (partially sintered) to liquid to solid. The consecutive melt steps were performed to evaluate the emissive behavior of the material during the solid-liquid-solid transitions. The temperature values reported by the pyrometer were compared with those from a type-K thermocouple available in the A2 system and that was embedded near the surface of the powder bed. Although the overall temperature trends for both devices were consistent, a faster response was achieved through the MW pyrometer, which also recorded higher temperatures at each preheating step. More importantly, this study provides in-process measurements of spectral emissivity as the temperature of the powder bed was progressively increased from room temperature (22 °C) up to ~900 °C, and during the seven consecutive melting steps. Raw data is captured and processed by the MW pyrometer to yield the target's spectral emissivity. Plots of spectral emissivity are produced for heating, melting and cooling. The measurement of the spectral response of emissivity for materials during processing conditions is a fundamental contribution that, to the knowledge of the authors, has not been previously addressed in PBF AM. Although future work will aim to understand and minimize the sources of uncertainty in the measurements reported, the results obtained indicate the dynamic (i.e. spectral and temporal dependence) nature of emissivity for the copper material used, which is likely a characteristic of other materials used in PBF AM. While not previously reported directly during PBF AM, this non-gray behavior has been seen in solid and liquid metal materials and alloys typically used in PBF AM, such as solid Inconel 718 [13,14], pure liquid titanium [15] and solid Ti6Al4V [16], further suggesting potential shortfalls associated with many of the thermal measurements reported in the AM literature. Enhancing the accuracy of radiation thermometry measurements can positively impact process control, component qualification, and the validation of computational models used to simulate PBF processes – all serving to motivate the current work described in more detail in the following.

2. Methodology

2.1. Electron beam powder bed fusion

The powder bed experiments were performed in an Arcam EB-PBF A2 system (Arcam AB, Sweden). The A2 system operates at a voltage potential of 60 kV with a maximum power of 3 kW and can attain a beam diameter that can continuously vary from 200 µm to 1000 µm. The A2 system has the ability to run in a high vacuum (i.e. 10^{-6}mBar); however, the regular EB-PBF process runs under a controlled vacuum of 2.0×10^{-3}mBar through a constant helium bleed, which were the conditions used in the current experiment. An enclosure of brushed stainless-steel walls (called the heat shield) is used during the process to reduce heat losses through radiation from the powder bed. The A2 system has a single grounded HKQIN-116 G type-K Inconel 600 sheathed thermocouple (Omega Engineering, CT, USA), with a probe length of 24 in. and 1.6 mm diameter, that is used as temperature feedback. This thermocouple has a standard accuracy of 0.75% of the temperature measured, for any temperature above 0 °C, as reported by the manufacturer [17]. During a normal build, the thermocouple is set in contact with the bottom of a metal plate that rests on the powder bed and is used as the fabrication substrate. The temperature readings from this thermocouple provide feedback throughout a build, informing and controlling the process using a proprietary algorithm. The intent of this work was to study the spectral and temperature-dependent emissivity behavior of powder particles as these particles experience heating, and eventually melting, solidification and cooling during PBF processing. As a result, the work presented here did not use a metal plate as a starting substrate. When using build plates in standard PBF processing, the build plate will likely influence the emissivity of the region under observation, during the initial stages of the build, given the small layer thickness (~50–70 µm) normally employed. These effects will be studied and presented in future work. For the current work, a leveled copper powder bed was prepared having the thermocouple embedded in it and located ~100 µm underneath the top surface of the bed. Side and top views of this setup are shown schematically in Fig. 1a). As mentioned previously, the Arcam A2 EB-PBF machine was used as a platform for experimentation that enabled measurements of the spectral emissive behavior of the material under study to be performed under prescribed scanning strategies (leading to the material experiencing heating, melting, solidification and cooling). The use of an electron beam to preheat the material drastically reduces the generation of spatter, as detailed in [18], and prevented contamination of the measurements due to the laser wavelength (typically ~1070 nm in L-PBF). Also, the vacuum environment in EB-PBF reduced impacts to the measurements due to environmental absorption of the emitted radiation, overall making EB-PBF a quite capable platform for the experiments.

2.1.1. Powder bed preheating

In the Arcam EB-PBF process, preheating of the start plate and of every layer is carried out by scanning with a defocused electron beam using a snake pattern that alternates its direction left to right or front to back after reaching a set number of scan repetitions. Several parameters of the electron beam dynamically interact to control the scanning strategy. Depending on the material and size of the substrate to be preheated, different values of beam current (mA), focus offset (mA), and beam speed (mm/s) are employed. Other parameters that control scanning include the line offset (mm), and two dimensionless numbers consisting of the number of repetitions and the line order parameter. Adjacent beam scan lines are separated by the value entered for the line order parameter. With the use of these parameters, the powder bed preheating is carried out more uniformly. During preheating, the material scanned by the electron beam radiates in the visible spectrum which permits visibility of the side-to-side scanning strategy, depicted in Fig. 1c). A lead-tinted window (covered with a movable shield) located on the front door of the Arcam machine, provides visible access allowing the operator to observe the process.

In the experiment performed in this work, gradual heating of the powder bed was accomplished using a custom preheating strategy involving fixed step increases of the beam current in a total of nine steps. The preheating steps were carried out in an area measuring 135 mm × 135 mm through direct scanning of the powder bed using the electron beam. The nominal parameters used for the electron beam were 25,000 mm/s beam speed, 80 mA focus offset, 1.2 mm of line offset and 20 for the line order parameter, based on the preheat theme for Ti6Al4V recommended by Arcam for 50 µm layers, except for the beam current. The beam current was varied from 5 mA to 45 mA in increments of 5 mA corresponding to the nine preheating steps. Each preheating step was timed and set to occur for ten minutes.

2.1.2. Powder bed melting

After the last preheating step (beam current of 45 mA) was completed, a series of seven consecutive melting steps were carried out on a circular region with a diameter of 20 mm that enveloped the region (~2.65 mm diameter spot) being measured by the MW pyrometer. Melting was carried out with the electron beam following a hatching strategy. The process parameters employed for melting of the copper powder were a beam scan speed of 500 mm/s, current and maximum current values of 10 mA, and focus offset of 20 mA. A speed function value of 15 and a top surface temperature of 390 °C were used, based on parameters reported in [19].

The pyrometer measurement region was selected to be approximately concentric with the circular area being scanned for melting (Fig. 1c)). These seven consecutive melting steps were used to examine the ability of the MW pyrometer to track the melt process and did not include deposition of layers of powder in between melts nor the layer preheating step used during the normal fabrication process. The technique further demonstrated the emissive behavior during repeated melting, solidification, and cooling (solid-liquid-solid transitions with the first melting step starting from powder).

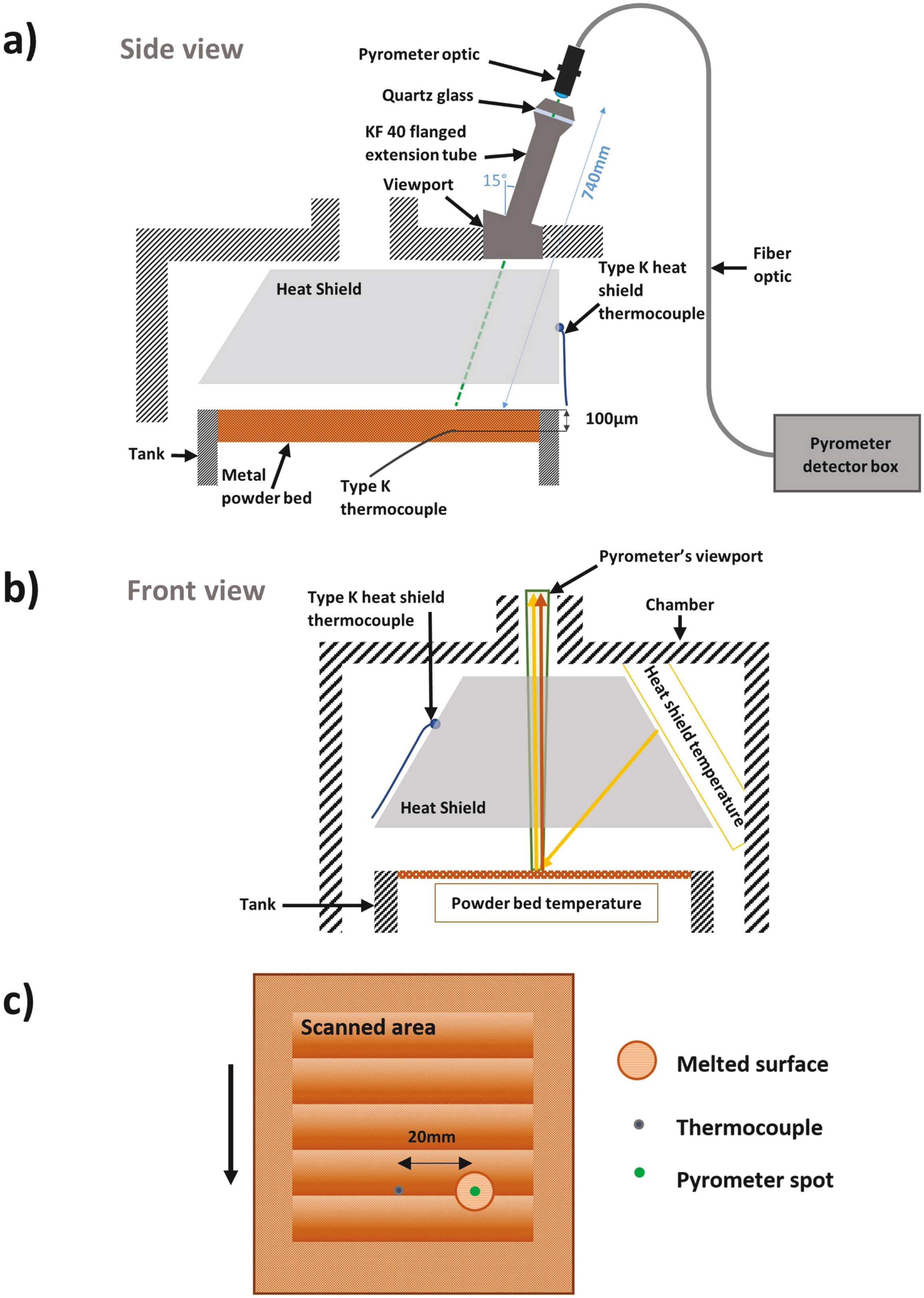

Fig. 1. Schematics showing the a) side and b) front views of the setup employed in the EB-PBF A2 system for the experiment, and c) schematic showing the preheat scanning strategy over the powder bed including an indication of the melted region. Note the distance between the measuring spots from the thermocouple and pyrometer (~20 mm).

2.2. Material

The material used for this experiment was high conductivity copper (HCCu) powder obtained from Sandvik (Sandvik Osprey Ltd., UK) with a particle size range of 45–100 µm (d50~75 µm) as per the powder specification from the provider. The powder had a 99.95% purity with a maximum oxygen content of 0.3%, as specified by the manufacturer [20].

Two HCCu copper powder lots were mixed to produce the 10 kg batch that was employed in the experiment. The mixture consisted of equal parts (5 kg) of powder lots 16D0323 and 16D0338. The mixing procedure was performed in a Turbula T10B (WAB Group, Switzerland) for 1 h.

The experiment was performed using copper due to its low electrical resistivity that enables direct powder preheating without electrically charging it and preventing the detrimental electrostatic powder ejection or "smoke" effect. Nonetheless, it is expected that the presented methodology can be directly applied to other materials used in PBF as a means to study emissive behaviors for these other materials during the rapid and non-equilibrium phase transitions experienced in PBF AM. Fig. 2a) and b) show 100 × and 700 × magnifications of the mixed powders observed by electron microscopy in a JEOL IT500LV (Tokyo, Japan) microscope.

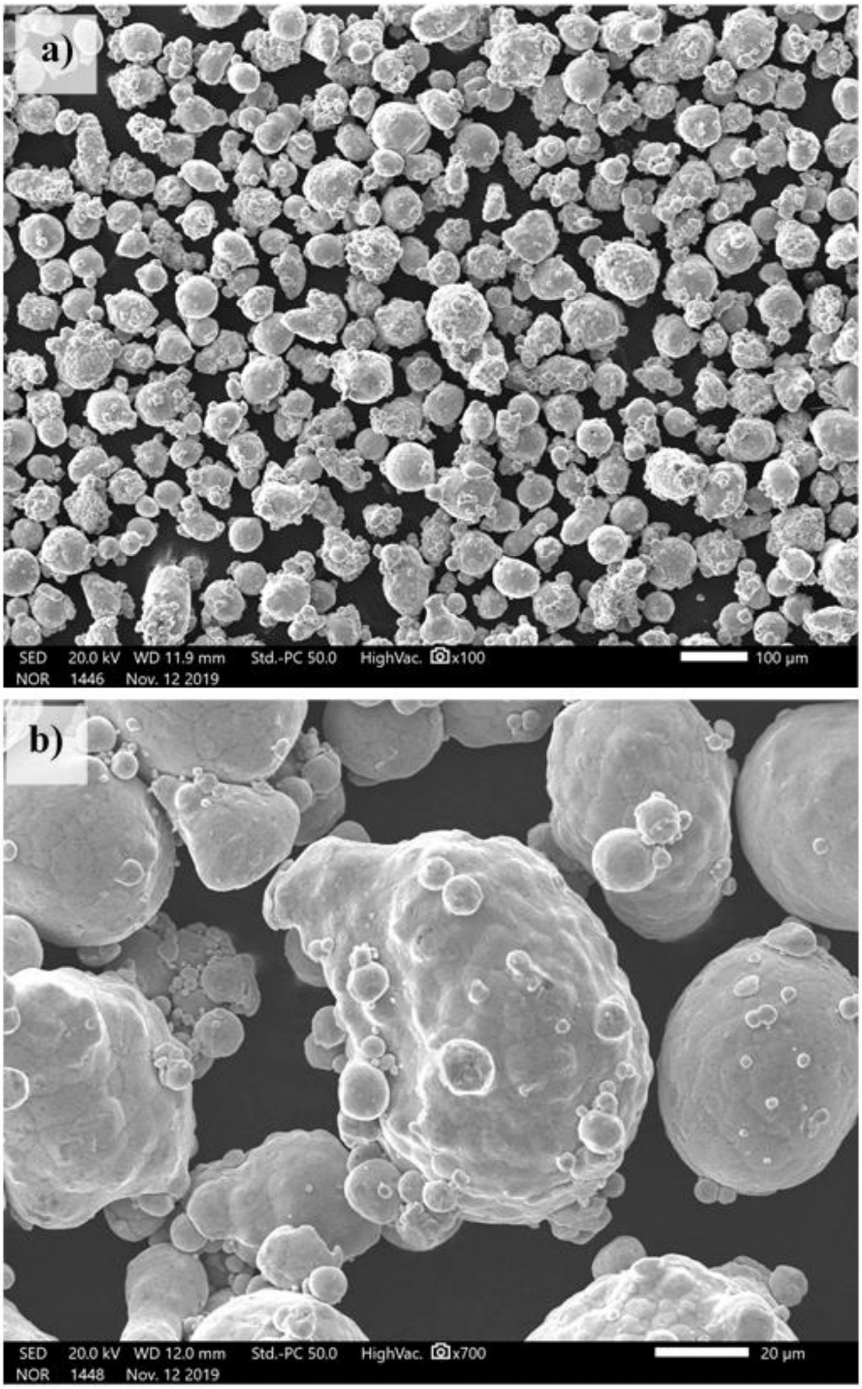

Fig. 2. Scanning electron images of the copper powder used to form the powder bed. a) corresponds to 100x magnification whereas b) is at 700x.

2.3. Pyrometry

To obtain the thermal signatures during the preheating of the powder bed, an FMPI Spectropyrometer (FAR Associates, OH, USA) was utilized. This MW pyrometer uses a 256-element Indium-Gallium-Arsenide (InGaAs) photodetector to resolve hundreds of ~2 nm wavebands in the spectral range of 1000 – 1650 nm [21], thus using hundreds of distinct, narrow wavelengths (wavebands). The device collects the entire spectrum simultaneously to avoid temporal bias. The instrument is delivered from the vendor with a calibration traceable to the National Institute of Standards and Technology (NIST). For this work, the units calibration was verified on site with a NIST traceable blackbody source (IR-563, Infrared Systems Development Corporation, FL, USA). Such calibration converts the uncalibrated detector output (raw intensity) to an actual spectral radiance measurement (corrected intensity). This corrected intensity over the spectrum is then used to calculate temperature based on Planck's distribution law [22]. The instrument has an accuracy of ± 0.15% for gray targets when measuring in the range of 500–2000 °C and ± 0.25–0.75% for non-gray behaving targets, as specified by the manufacturer [23]. As will be described in the following, it is the ability of this instrument to measure and analyze targets' non-gray as well as gray behaviors that make this instrument and method valuable for the advancement of accurate surface temperature measurements in PBF.

For the temperature computation, the FMPI pyrometer uses an algorithm that removes anomalies by analyzing the spectrum recorded, and disregards the corrected intensities that do not exhibit thermal (Planckian) behavior [24]. After this decision process is performed, the selected corrected intensity data over the wavelength spectrum is used to calculate a matrix of temperature values by employing the ratio solution of Planck's law for multiple intensity-wavelength pairs [22]. The temperatures in the matrix are averaged and the corresponding standard deviation is analyzed; if the standard deviation is deemed acceptable, the average temperature and its standard deviation are recorded. Otherwise, the algorithm performs a check for non-graybody behavior (i.e. spectral variation of target emissivity) and corrects individual temperatures in the temperature matrix to account for this variation. Following the non-gray correction, the temperature matrix is recalculated, and the average temperature and its standard deviation (referred to as tolerance by the manufacturer) along with several other parameters are recorded in a log file (spreadsheet). For every temperature measurement reported, the FMPI pyrometer stores a data file with raw and processed information consisting of raw intensity, dark count (background noise), corrected intensity, and emissivity values at each wavelength used. The emissivity values captured in the stored files were used to construct plots of spectral target emissivity (1080–1640 nm) at the various process temperatures, as discussed further in Section 2.5. The temperature determination procedure, including the compensation for non-graybody behavior, is detailed by Felice [22]. Outside the realm of AM, this instrument has been extensively validated against measurements from immersion thermocouples during vacuum induction melting (VIM) of nickel superalloys, stainless steels, titanium, and titanium alloys [25,26]. For example, extensive comparison of Type-R immersion thermocouples and the MW pyrometer were shown to agree within their stated accuracy in VIM processing of many different nickel superalloys [25].

For this work, the FMPI pyrometer used optics with a measurement area (spot) size of ~2.65 mm at the focal length of 762 mm. The size of the spot is relatively invariant with modest changes in operating distance. Although the measurement spot is large in relation to the meltpool [27], the FMPI can directly observe the temperature of molten (liquid) material depending upon the local temperature gradient. It has been demonstrated that compared to single color pyrometers, two-color pyrometers have markedly lower sensitivity to uneven radiance of the target [28], as is expected in EB-PBF due to the traveling heat source radiating more than powder or solidified materials within the target. This insensitivity greatly minimizes the error in the temperature calculation when using a ratio pyrometer, including the FMPI [29]. For aiming, the pyrometer projects a laser spot to clearly locate the measurement region. The same optics are used for projection and measurement, removing potential positioning error. The end optic consists of a lens assembly that focuses radiation onto the core of a fiber optic cable, which is connected to the FMPI pyrometer detector box. In this work, measurements were taken by locating the FMPI pyrometer optic at 15° from the normal vector of the powder bed (Fig. 1a)). This observation angle has no effect on the measurements other than elongating the axis of the measured spot in the direction of measurement. According to the manufacturer, angles as steep as 85° from the normal do not change the temperature result, while angles beyond 30° can have an effect on the observed signal strength or emissivity [8].

2.3.1. Spectral emissivity

As mentioned in the previous section, the stored data files report the signal strength (or target emissivity as used here) values throughout the wavelength range of the FMPI pyrometer for each temperature measurement recorded in the log file. To calculate the emissivity values, the device uses a form of Planck's distribution law (Eq. (1)) [24].

$$\varepsilon = \frac{L\lambda^5\left[e^{hc/\lambda k_B T} - 1\right]}{2hc^2} \tag{1}$$

In this expression, the intensity values measured and corrected by the FMPI pyrometer (available in the stored data file) are taken as L and the average temperature calculated as T. The constant values for c, h and k_B are the speed of light in a vacuum (2.998×10^8 m·s^{-1}), Planck's constant (6.626×10^{-34} J·s), and the Stefan-Boltzmann constant (1.381×10^{-23} J·K^{-1}), respectively. The wavelength values (λ,nm) and spectral emissivity of the target is recorded for the full spectral range of the instrument. Changes for the speed of light under vacuum versus air have been ignored and their impact on the emissivity calculation can be considered negligible given the speed of light in vacuum and in air varies by only ~0.03%. Data from the raw files were manipulated and processed using custom scripts developed in MATLAB® 2019b (MathWorks, MA, USA) to plot the spectral emissivity values at different temperatures.

2.3.2. Acquisition rate

The FMPI pyrometer has a self-adjusting exposure time dependent upon the raw intensity; the overall data acquisition rate (repetition or log rate) is, in turn, dependent upon the exposure time, calculation overhead, and other factors. The pyrometer calculates and reports a single temperature measurement once an adequate signal is achieved with an acceptable signal-to-noise ratio. In general, the higher the target temperature, the faster the data acquisition rate. The manufacturer reports a minimum exposure time of 4μs with a minimum acquisition period of 40 ms. For this experiment, the exposure times varied in the range from 18 ms up to 8 s, while the temperature acquisition rate was computed from the data to be in the range of 0.125–23 Hz. Although our group is exploring methods for improving the acquisition rate of the MW pyrometer, the current acquisition rate is similar to or better than most thermocouples; those used in this study have response times ranging from approximately 3 ms to 2.1 s, depending on the sheathing thickness [30]. Obviously, the significant added benefit of non-contact measurement provided by the MW pyrometer enables its use in the extreme temperature environment such as the one in the EB-PBF system.

Although the FMPI pyrometer is practical for use in PBF AM, the acquisition rate obtained in this study is still comparatively low compared to other MW sensors. For example, Dagel et al. created a multi-wavelength pyrometer using four sCMOS cameras with different bandpass filters to perform ratio pyrometry for temperature measurements on laser welding and laser-based AM. The acquisition rate reported for the detector was as high as 60 Hz in the wavelength range from 400 to 1000 nm [31]. Similarly, Doubenskaia et al. reported the development and use of a multi-wavelength pyrometer with 12 channels for temperature measurement in laser cladding applications [32]. This detector was reported to have a minimum exposure time of 50μs with a spectral range of 1.0–1.5 μm. Other published works from the same group reported measurement of temperatures in L-PBF, yet their work did not provide a discussion of the acquisition rate of the device [33–36]. The optical assembly featured in these studies is for measurements on the axis of the laser, attached directly to the scanner of the L-PBF machine. However, it should be noted that these faster MW devices use many less channels than the instrument used in this study. Using less channels and wider wavebands, the exposure times can be reduced as more radiant intensity is available for sensing. This leads to trade-offs between acquisition rates and accuracies depending on available radiant intensity for sensing within each of the waveband limits (all within the constraints of the available sensing and hardware technologies).

Multi-wavelength pyrometry has also been used extensively to perform temperature measurements on other complicated environments where direct contact measurements were not possible. For example, Montgomery et al. reported the development of a seven channel multi-wavelength pyrometer that was used in measuring fast temperature changes and to obtain phase transformation data for various materials, such as palladium hydride (PdH), heated up by lasers inside diamond anvil cells. The detector used Indium-gallium-arsenide (InGaAs) and pure gallium (Ga) sensors operating in the wavelength range from 800 to 2200 nm with a reported acquisition rate in the range of 1–70 kHz, which the authors state was limited by their analog-to-digital converter [37]. The study by Wang et al. reported the use of an 8 channel multi-wavelength pyrometer with silicon (Si) and InGaAs sensors. The pyrometer was capable of reading temperatures from 1500 K up to 15,000 K in a wavelength range from 500 to 1650 nm [38]. The acquisition rate of the pyrometer was equivalent to that of the individual sensors (either Si or InGaAs) employed, corresponding to 50 MHz or 150 MHz, respectively.

In comparison to most of the multi-wavelength detectors employed in the research described above, the FMPI pyrometer can be considered a practical approach for monitoring in EB-PBF. First, the end optic of the FMPI pyrometer can be easily integrated into current generation EB-PBF systems to carry out measurements. Also, the FMPI pyrometer is calibrated against the blackbody source offline (by the manufacturer or on the user if desired) and readily used afterwards. The alternative approaches described above involve more complex component assemblies, such as the need for inline blackbodies that make integration within an EB-PBF machine more challenging. The most prominent advantage of the FMPI pyrometer is its spectral response. The plethora of data in the spectral range made up of a large number of wavebands with very narrow bandwidths enables it to determine and correct for non-graybody behavior and analyze the data captured to discern and discard spectral domains where plasma emissions, or environmental absorptions are present [21]. By comparison, other detectors described in literature [31–38] only acquire data from a limited number of broad wavebands and are therefore unable to perform such a detailed analysis.

2.3.3. *Optical path*

As indicated previously, EB-PBF involves processing at or lower than 10^{-3}mBar vacuum levels and elevated temperatures. This makes it challenging for directly attaching sensors inside the processing chamber because most sensors' electronics cannot withstand these extreme temperature and vacuum conditions. For this reason, the FMPI pyrometer was attached outside the machine looking into the chamber through an available viewport. The setup was improved from that previously described in the works of Minjares and Cordero et al. [11,12]. While Minjares used this external setup to measure temperatures during processing of a Ni-based alloy in an Arcam S12 EB-PBF system, Cordero et al. measured temperatures for Ti6Al4V while processing in the same A2 system used in our work. In both prior studies, the setup resulted in metallization of the quartz glass in the viewport, reducing and eventually stopping the acquisition of signals by the pyrometer [11,12]. The detrimental impact on acquisition of data was evident as soon as a couple layers were processed, as reported by [11]. With the use of radiation thermometers, as is the case with the FMPI pyrometer, the reduction of the transmission due to metallization will cause the loss of calibration, thus negatively impacting the accuracy of measurements.

In the current work, the experimental setup included the development and installation of a vacuum rated extension tube that prevented metallization of the quartz and thus enabled near-continuous measurements without loss of accuracy. Metallization of the window material is a significant issue since the resulting transmission is not spectrally uniform. By Kirchoff's law, the transmissivity and reflectivity of a material add to one. Thus, when the material being processed is a non-gray metal the deposition on the window is also non-gray. The resulting deposition will cause inaccuracy for any type of pyrometer. The extended tube provided sacrificial area where metal vapor condensed before reaching the quartz glass. An available viewport, situated atop the chamber of the Arcam A2 system (Fig. 1a), was fitted with a custom-built stainless-steel fixture unto which an assembly was attached that consisted of two sections of high-vacuum rated KF-40 flanged tube. The tubes had nominal lengths of 320 mm and 130 mm to account for the focal distance of the FMPI pyrometer end optic, and they were coupled using available vacuum clamps. Once the KF-40 tubes were attached to the stainless-steel fixture, the total distance of this extension assembly was 450 mm (with an L/D of 11.25). The quartz glass was a 6 mm thick GE 124 window (QSI Quartz scientific, OH, USA), and it was attached to the KF-40 flanged fitting using Torr seal (Agilent Technologies, Inc., CA, USA), which is a vacuum rated cement. Quartz was used as it provides a steady transmission (neutral density) of ~94% over the wavelength range of the FMPI pyrometer. The 6% loss in transmission was accounted for with the calibration of the FMPI pyrometer against the blackbody source (described in Section 2.3.5), by including the quartz glass used for the experiments. Once the assembly containing the fixture and extension tube was installed, the end optic of the FMPI pyrometer was located concentric to the tube, with a gap of 5 mm from the quartz glass. The end optic (S/N: 13249-1) consisted of an optical assembly with a focal length of 762 mm, as specified by the manufacturer (FAR associates, OH, USA).

2.3.4. *Alignment*

For the experiment reported here, the FMPI pyrometer was aimed at a single, distinct spot or small region within the powder bed. The setup was prepared by starting with the formation of a flat powder bed in which initially the tip of the thermocouple was exposed and approximately level with the surface of the powder. Then, using the tip of the thermocouple and the green laser spot projected by the FMPI optic as visual indicators, the measuring spot of the pyrometer was located at ~20 mm to the side from the location of the thermocouple tip (Fig. 1c)). Once both the thermocouple and pyrometer were aligned relative to each other, the powder bed was lowered 100 μm and a fresh layer of powder raked across. This method ensured that the thermocouple tip was embedded ~100 μm below the powder bed throughout the experiment, and thus able to provide temperature readings sufficiently close to the exposed surface of the powder bed. Correspondingly, the pyrometer was observing directly on the top surface of the powder bed at an angle of 15° from the surface normal. The offset introduced between the location of the thermocouple tip and the measuring spot for the FMPI pyrometer was intentional and used to minimize heat conduction through the body of the thermocouple that would impact the temperature readings for the pyrometer's region of interest or target.

2.3.5. *Multi-wavelength pyrometer calibration and verification*

To maintain the accuracy specified by the manufacturer, a calibration using a National Institute for Standards and Testing (NIST) traceable blackbody source (IR-563, Infrared Systems Development Corporation, FL, USA) was performed. The first step of the calibration process consists of calibrating the FMPI while recording the blackbody source at the steady state temperature of 1000 °C. Then, the calibration is verified by lowering the temperature of the blackbody source to 500 °C and confirming the values captured at this steady temperature. Afterwards, a final verification step was performed at five more temperatures, starting at 600 °C, followed by increments of 100 °C, up to 1000 °C. The calibration and verification processes were performed before carrying out the powder bed preheating experiment reported here, using the same optical path (GE 124 quartz glass) as that used during experiments to remove signal transmission losses due to the optical path. However, the calibration was performed in open environment conditions (~30% relative humidity), different from the vacuum environment where the experiments were performed. The impact that this may have on temperature and emissivity calculations was assumed to be negligible due to the ability of the FMPI pyrometer to exclude sections of the spectrum that do not emit following Planckian behavior during the temperature calculation step [24].

As can be seen in Table 1, the largest standard deviation reported by the device during the blackbody calibration assessment was ± 1.28 °C for temperatures in the range from 500 °C to 600 °C. Also, the general trend observed during this calibration verification process indicated that standard deviation decreased as the temperature of the blackbody increased except for the highest temperature of 1000 °C. The smallest tolerance was ± 0.30 °C at a temperature of 900 °C. The table also shows the measured signal strength (emissivity) for the blackbody source at the wavelength of 1500 nm, reported to three decimal places, with values that remained within the expected emissivity of 1.000. Column 2 in the Table 1 shows the calculated uncertainty for the temperatures of the blackbody.

2.3.6. *Temperature sampling and calculations*

During the preheating experiment that was conducted, continuous measurements of temperature were recorded by the FMPI pyrometer in steps lasting ten minutes. From each steady state step, three temperatures were sampled and used for the calculations used for computing the radiation contribution ratio (R), as shown in Section 2.4. These values were also used for sampling of spectral emissivity calculated by the FMPI pyrometer discussed in Section 2.5. The temperatures sampled including the median (the temperature occurring exactly at the five-minute mark in each preheating step), and two more temperatures sampled one minute before and one minute after the median. The mean temperatures reported at each preheating step correspond to average values calculated by selecting temperatures occurring in the range spanning from one second before to one second after the median and hence include a measure of the standard deviation as listed in Table 2.

Table 1
Values obtained during calibration and verification of the FMPI pyrometer against a blackbody source.

Blackbody Set Temperature[a]	Uncertainty in blackbody temperature	Before experiment	
		Pyrometer reading (Temperature ± FMPI Tolerance)	Pyrometer reading (Signal Strength)
500 °C	3.0	501.9 ± 1.28 °C	1.000
600 °C	3.1	602.8 ± 1.28 °C	1.000
700 °C	3.2	702.8 ± 0.95 °C	1.000
800 °C	3.3	802.5 ± 0.51 °C	1.001
900 °C	3.5	901.7 ± 0.30 °C	1.002
1000 °C	3.6	1000.2 ± 1.12 °C	0.997

[a] Temperatures reported for blackbody are within the uncertainty specified by the manufacturer (± 0.2 °C).

2.4. *Radiation environment contribution*

Temperature measurements using non-contact methods usually involve an analysis of the radiative surrounding environment to account for its effect on the temperature measurements. To evaluate the radiative environment on the measurements, the temperatures for two walls of the heat shield assembly of the Arcam A2 system were continuously measured during the length of the preheating experiment. Following the method presented by [1,2], the temperatures of the heat shield walls were measured by attaching spot welded tip GG-K-24 type-K thermocouples (Omega Engineering, CT, USA) to the front and side heat shield walls at the center location of the heatshield, as depicted by Fig. 1a). The attached thermocouples were inserted into the vacuum chamber using an ISO-KF NW 16 120XTK016–5-S type-K thermocouple feedthrough (Pfeiffer Vacuum Inc., Boston, MA). The measurements from these thermocouples were recorded using an NI-9214 temperature input module with a cDAQ-9171 chassis (National Instruments, TX, USA).

For this analysis, the assumption was made that the temperature captured by the thermocouple attached to the side heat shield wall could be used as an approximation of the mean radiant temperature of the heat shield enclosure. The work by Rodriguez et al. reported a mean radiant temperature 27 °C lower than the side heat shield. In our work, the highest shield temperature measured was ~355 °C which was similar to the ~368 °C value reported by [1]. Fig. 1b) depicts how the radiation emission from the heat shield reaches the powder bed. As temperature was elevated due to the increased preheating, the heat shield temperature also increased, with parts of these reflected emissions absorbed by the powder bed and reflected into the FMPI end optic by the powder bed itself, as indicated by yellow arrows in Fig. 1b).

The contribution of the EB-PBF radiative environment (brushed stainless-steel heat shield walls) on the pyrometer measurements was approximated using Planck's Law to calculate a ratio of the spectral radiance of the heat shield (L_{HS}) to that of the powder bed (L_{PB}) using the expression below. This assumes blackbody (i.e. maximum possible) emission from the heat shield walls and from the powder bed into the pyrometer:

$$R\% = \frac{L_{HS}}{L_{PB}} = \frac{\frac{2hc^2}{\lambda^5} * \left(e^{\frac{h \cdot c}{\lambda \cdot k_B \cdot T_{HS}}} - 1 \right)^{-1}}{\frac{2hc^2}{\lambda^5} * \left(e^{\frac{h \cdot c}{\lambda \cdot k_B \cdot T_{PB}}} - 1 \right)^{-1}} \tag{2}$$

Where h is Planck's constant, k_B is Boltzmann constant, c is the speed of light, λ is the wavelength (m)–all of them with units in the SI system–and the temperatures in Kelvin for the heat shield (T_{HS}) and for the powder bed (T_{PB}). With this equation, the ratio of contribution was calculated at each preheating step by using the steady median temperature of the powder bed captured by the pyrometer and the corresponding temperature of the heat shield wall. The analysis was performed in the spectral range of the FMPI pyrometer (i.e. 1080–1640 nm).

The ratio calculation was made assuming perfect reflection, and emission from a blackbody (i.e. emissivity $\varepsilon = 1$) and then by imposing emissivity values for brushed stainless steel with an $\varepsilon = 0.36$ [14], the emissivity of copper obtained in situ, and reflectivity values from the copper ($r = 1 - \varepsilon$). However, it should be pointed out that, for this experimental setup, these ratio values will decrease even further if emissivity and reflectivity values for the copper powder bed, plus the radiation view factors from the heat shield enclosure to the powder bed, and from the powder bed to the pyrometer end optic piece, are all taken into account.

Table 2

FMPI pyrometer temperature measurements used for each powder bed preheating step. Temperatures in columns 2, 3 and 4 have the temperatures ± the FMPI tolerances reported. The values before and after the median were taken 1 min from the median. The values in column 5 are the mean of all the values within a span of 1 sec before and after the median to accomodate for the oscillation of temperature, accompanied by its corresponding standard deviation.

	Temperatures			
Preheating Step	Median (Temperature ± FMPI tolerance)	Before median (Temperature ± FMPI tolerance)	After median (Temperature ± FMPI tolerance)	Mean (average Temperature ± standard deviation)
1	610.0 ± 1.89 °C	611.1 ± 1.91 °C	610.0 ± 1.87 °C	609.9 ± 0.8 °C
2	731.4 ± 1.11 °C	731.7 ± 1.10 °C	730.9 ± 1.12 °C	737.0 ± 4.2 °C
3	786.9 ± 1.23 °C	796.0 ± 1.04 °C	784.4 ± 1.22 °C	785.7 ± 5.1 °C
4	827.5 ± 1.78 °C	834.8 ± 1.70 °C	821.4 ± 1.71 °C	827.8 ± 5.3 °C
5	834.4 ± 1.45 °C	839.9 ± 1.40 °C	825.9 ± 1.48 °C	831.5 ± 5.8 °C
6	842.4 ± 0.96 °C	835.3 ± 1.01 °C	835.9 ± 0.97 °C	841.1 ± 6.1 °C
7	875.3 ± 0.55 °C	871.8 ± 0.64 °C	883.1 ± 0.44 °C	875.5 ± 7.2 °C
8	918.1 ± 0.32 °C	911.1 ± 1.35 °C	905.6 ± 1.82 °C	910.8 ± 8.9 °C
9	949.7 ± 0.90 °C	954.0 ± 2.35 °C	953.1 ± 0.38 °C	941.2 ± 7.9 °C

2.5. *Device synchronization*

The logged values from the FMPI pyrometer, the thermocouple in the powder bed, and from the thermocouples attached to the heat shield walls provided a time stamp that could be used for tracking and correlating the measurements amongst instruments. Before experimentation, the timestamps of all the devices used were manually synchronized to the computer logging the data from the FMPI pyrometer.

3. Results and discussion

3.1. *Temperature measurements*

3.1.1. *Preheating steps*

Fig. 3a) shows a plot of the temperature values recorded by the FMPI pyrometer (black circles), the thermocouple underneath the powder bed surface (gray circles), the thermocouple attached to the front heat shield (gray triangles), and side heat shield (black triangles) throughout the length of the experiment. Colored boxes are included in the figure to help the reader identify the different steps of the process (pre-heat, melt, and cool down), as identified in the legend. Nine steps are clearly visible in the temperature plot corresponding with each preheating step. This plot indicates that the FMPI pyrometer captured higher temperature values compared to the thermocouple; this effect can be explained by the fact that the thermocouple was measuring ~100 μm below the surface of the powder bed whereas the pyrometer was measuring directly on the exposed surface of the bed, as schematically shown in Fig. 1a).

Using a simple 1-D steady-state conduction model, it was determined that 100 μm of powder (with an assumed thermal conductivity of 0.232 W/m-K, as described by [39] for 75 μm diameter Cu powder) would decrease the readings from the thermocouple by 28–63 °C, depending on the temperature of the surface (i.e. the preheating step). Nevertheless, similar overall behavior was shown by both instruments, as shown by Fig. 3a), and although there were differences in location and time response, the thermocouple measurements helped support that the FMPI was accurately capturing the surface temperature. This conclusion will also be supported throughout the discussion of the results that follow.

The regions indicated with small boxes and arrows in Fig. 3a) correspond to amplified sections of the third (Fig. 3b)) and seventh (Fig. 3c)) preheat steps demonstrating a fluctuation behavior in temperature that is evident for these and every preheating step. The origin of this fluctuating behavior of the measurements was related to the scanning strategy of the electron beam which can be thought of as subsequent heat transfer fronts advancing through the powder bed. For this, an analysis was conducted to examine if the period in the temperature plots matched the time it took the preheat front generated by the electron beam to cycle and pass over the measurement region of the FMPI pyrometer. The total time it takes for the electron beam to scan the preheat area was calculated using the scanning parameters described previously (Section 2.1.1) and it resulted in a time of 0.6 s. This time corresponds to the period measured from the pyrometer signal peaks shown in both Fig. 3b) and c) which was 0.61 ± 0.06 s; considering a total of 17 measurements over 10 s elapsed at 3500 s of the experiment.

3.1.2. *Melting*

Towards the end (right) of the plot in Fig. 3a), there are seven melting events depicted as seven consecutive peaks. These seven melt events, shown in the expanded view in Fig. 4a), were executed by the A2 system with no powder spread during the raking time in between scans. The data indicate that the melting point for copper (~1084 °C) was exceeded in every melting event with the maximum and minimum temperatures of individual peaks measured at 1277 °C and 1103 °C, respectively. Further, there was an overall decreasing trend observed by the FMPI pyrometer during these melt events, as shown in Fig. 4a). This behavior can be explained given that no powder deposition occurred in between each of these melting steps, and the increasing volume of solidified material after each melt scan resulted in larger lumped-capacitance that effectively increased heat capacity after every subsequent scan, as shown by the decreasing trend in temperature in Fig. 4a). However, the peak temperatures measured may be lower than the actual maximum temperatures reached during the melting due to the self-adjusting exposure time feature of the FMPI. This does not refer to a lack of accuracy but rather sparse data in rapidly changin thermal environments, as the FMPI's algorithm determining the acceptable signal-to-noise ratio requires computation time and limits acquisition rates. Ongoing work in this area is focused on developing methods for improving data resolution within the melt region. The span in between peaks corresponded with the time involved in the regular raking step (~14 s), although no powder deposition was performed, so each melt after the initial melt is a re-melt event. Further, the 14 s time in between melts served to provide a very effectively resolved cool down region.

3.1.3. *Heat shield temperatures*

The experimental setup allowed for measurements of the temperatures of two heat shield walls using type-K thermocouples as described in Section 2.4 and depicted in Fig. 1. Fig. 3a) includes the plot for the temperature of the side heat shield wall, shown in light gray. This plot shows a steady increase from room temperature up to about ~310 °C (at the 3000 s mark) followed by a second region with a lower temperature slope that reached a maximum temperature of ~354 °C (at ~5500 s) before preheating was stopped. At this point in time, the corresponding powder bed temperature captured by the FMPI pyrometer was ~960 °C. The temperature values captured for the front heat shield wall remained below those of the side heat shield, as can be seen in Fig. 3a).

3.1.4. *Acquisition rates*

The high scanning speeds of the beam (~500–2000 mm/s) in EB-PBF

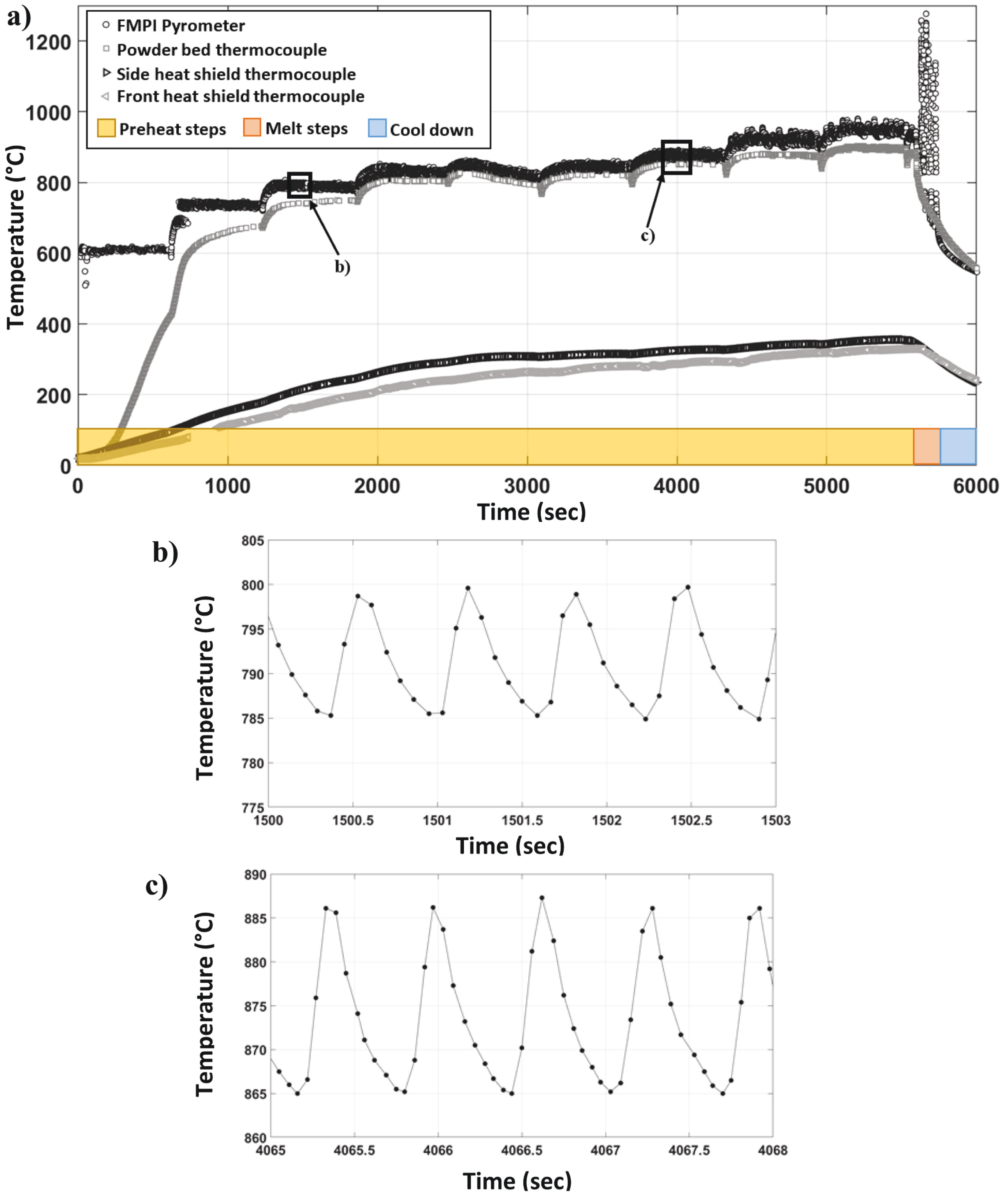

Fig. 3. **a)** Plot of temperatures values acquired by the FMPI pyrometer (black), thermocouple embedded in the copper powder bed (gray), and thermocouple attached to the side heat shield (light gray). **b)** and **c)** correspond to zoomed in regions in steps three and seven, to indicate the fluctuating behavior of the measurements acquired. Colored boxes in a) are intended to help the reader identify the different heat transfer steps (pre-heat, melt, and cool down).

can lead to non-equilibrium solidification, requiring the use of thermal radiation sensors with high acquisition rates to capture this transient temperature behavior. Devices with an acquisition rate in the range of MHz or higher are required to measure cooling rates, as these have been reported on the order of 10^5–10^6 K/s [40–42]. The use of radiation thermometry devices operating in the MHz range could also provide valuable information of the solidification dynamics as the reported values for solidification rates in the L-PBF process are in the range of 300–800 mm/s [42].

The overall acquisition rates obtained in the experiment were as low as ~2 measurements per second at relatively low temperatures (~600 °C) to ~23 measurements per second at the highest temperatures

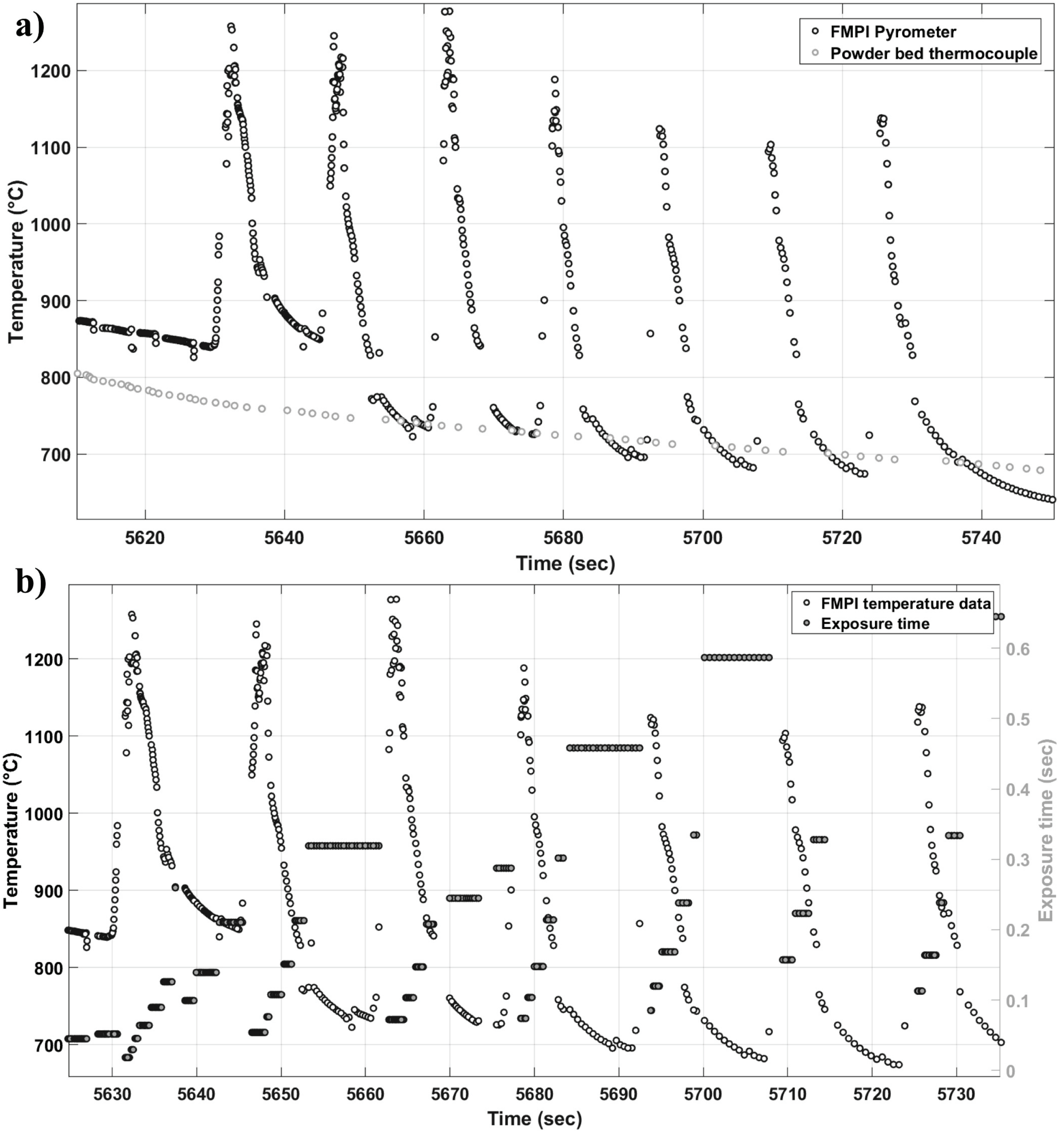

Fig. 4. a) Close-up view of the temperature signals captured by the FMPI pyrometer during seven consecutive melting steps performed without preheating and without powder deposition. b) Temperature acquired (left) with secondary y-axis (right) for pyrometer exposure time (illustrating the effect of the FMPI's algorithm changing acquisition rate based on S/N ratio).

measured (∼900 °C), as shown in Fig. 5a). Correspondingly, the acquisition rates during melting spanned from ∼3–20 measurements per second in the temperature range from ∼1000–1200 °C.

As discussed previously, the FMPI pyrometer automatically adjusts the exposure time to accommodate the intensity of the target radiation. The acquisition rate is determined by the sum of the exposure time and the time to process the data collected. The theoretical upper limit of acquisition rate for the FMPI is 25 Hz. The lower limit is governed by the exposure time, which can be as long as several seconds at the lowest temperatures, where radiance is greatly reduced.

The plots of Fig. 5a) and b) show acquisition rates and exposure times, respectively, as a function of temperature. Ongoing research will aim at minimizing the calculation overhead so as to approach the 100 kHz theoretical limit of acquisition rate.

3.2. *Radiative environment contribution*

Type-K thermocouples were used to take temperature measurements

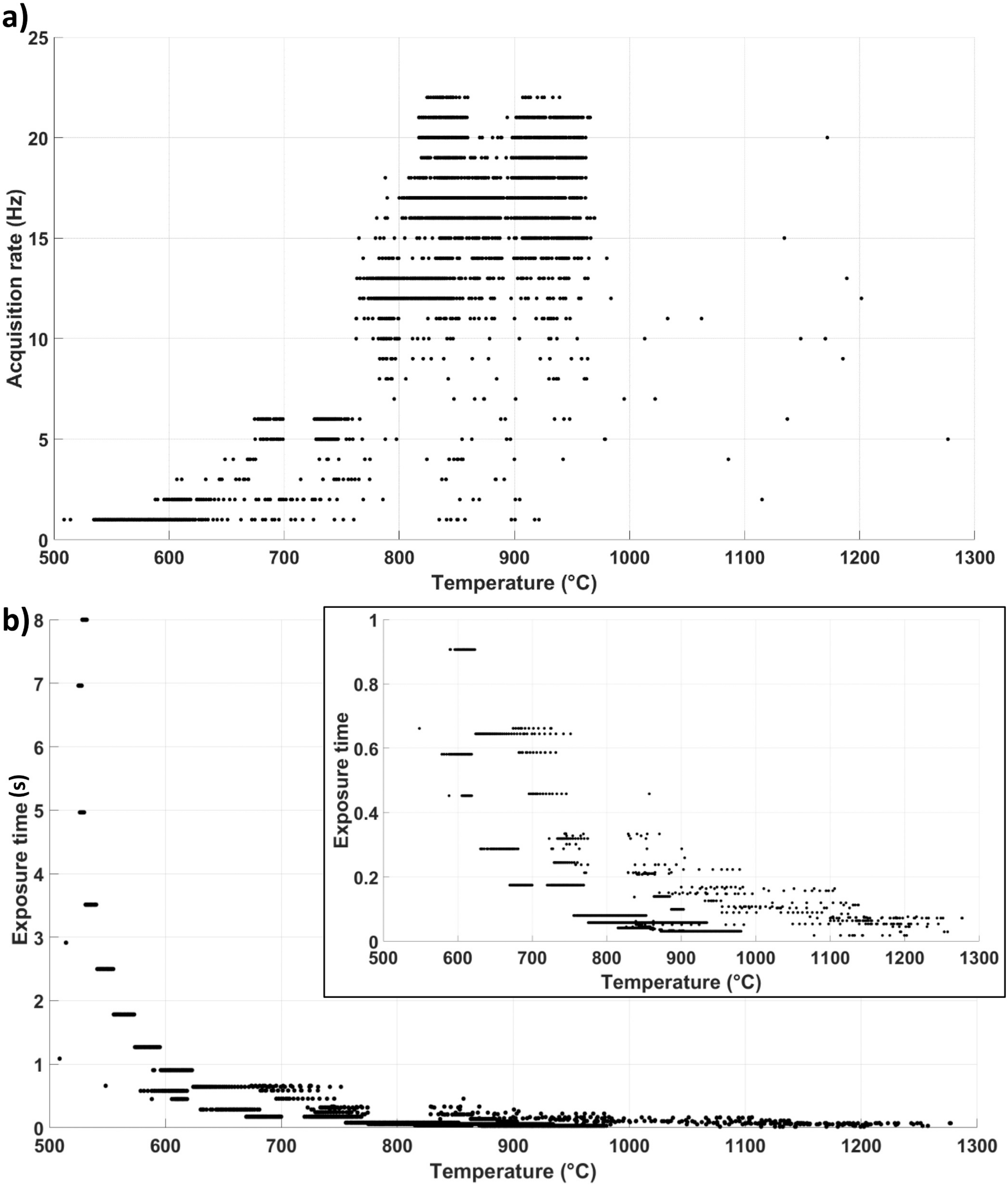

Fig. 5. **a)** Acquisition rate in Hz over temperature recorded. The acquisition rate was obtained by taking the reciprocal of the difference between time signatures at each data point obtained. **b)** Exposure time against temperature obtained during the experiment (close-up limits the y axis from 0 to 1).

of one of the side walls and the front wall of the heat shield enclosure of the Arcam A2 system. The plot for the temperatures for the heat shields is shown in the two light gray plots in Fig. 3a) indicating that the temperature peaked at ~354 °C, similar to the temperatures measured for Ti6Al4V in [1]. Given the relatively low temperatures reached by the heat shield walls (Fig. 3a)), it is expected that their contribution is small in the measurements obtained by the FMPI. The study by Ruffino used ratio pyrometry to measure hot spots of a surface under non-isothermal planar conditions and the influence of cooler spots. His results indicated that the effects in the measured temperatures due to spots of the surface

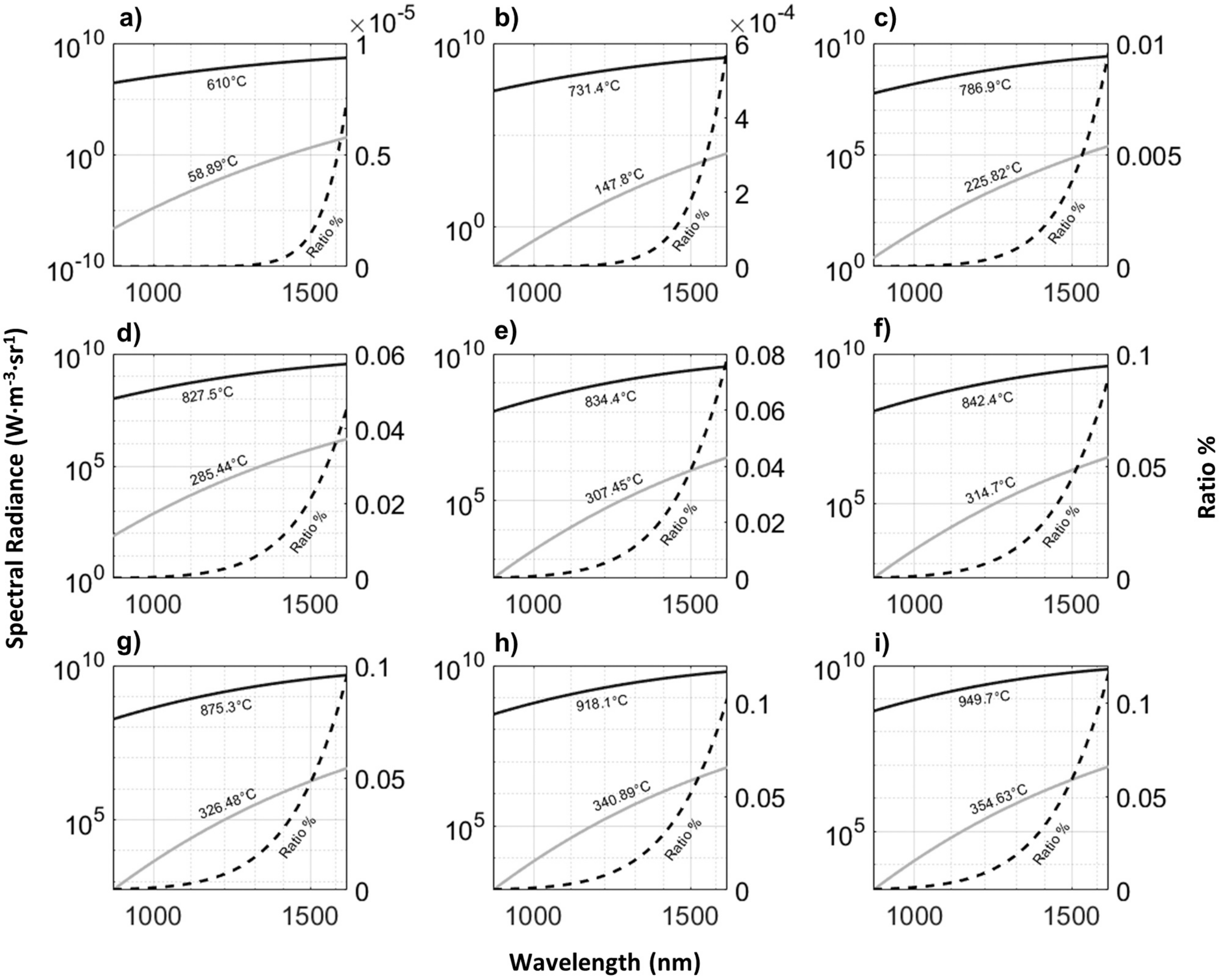

Fig. 6. Planck radiance curves over the working wavelength of the FMPI for the temperatures shown at the nine preheating steps corresponding figure parts a) through i). The black curve represents the temperature of the powder bed. The gray curve represents the temperature of the heat shields. The black dashed curve represents the percent ratio of the spectral radiance at each wavelength.

at lower temperatures could be considered negligible until the two temperatures were within ~200 °C; outside this range, errors in measurements were below a single digit of temperature [28]. In our work, the contribution from the heat shields can be assumed negligible as the temperature difference between the target and the heat shield walls exceeded 400 °C during the length of the experiment, as shown by Fig. 3a). The set of plots in Fig. 6 show the ratios of spectral radiance contribution at each preheating step, using the median temperatures in Table 2 for the pyrometer and the corresponding temperatures for the heat shields. The plots indicate the spectral or wavelength dependency of the ratios. Temperature values are shown for reference only.

The maximum ratio of contribution was ~0.125% belonging to the ninth preheating step (at the corresponding powder bed temperature of 934.8 °C). This contribution was considered negligible since the theoretical contribution of 1% of the ratio to the maximum temperatures measured was calculated to be ~5 °C. This contribution could be included when considering more accurate surface temperature measurements, following the method outlined in [1].

3.3. Spectral emissivity plots

3.3.1. Preheating steps

During preheating, the variation of the emissivity for the heated copper powder over the spectral range from 1080 to 1640 nm was measured as temperature was increased. The spectral emissivity plots (shown in Fig. 7) indicate that the emissivity was spectrally (i.e. wavelength) and temporally dependent, and it also indicated the non-graybody behavior for the copper powder used. The temporal dependence is evident in the plots for preheating steps 8, and 9 ((Fig. 7h) and i)), where large variations in the measured emissivity spectra are observed for the three sampled temperatures at each preheating step. These variations were measured in the range from 10% to 15% when comparing individual values in the three spectrums of a given plot. For the rest of the preheating steps (i.e. a), b), c), d), e), f), and g)), the emissivity values are clustered within tighter ranges and they exhibit reduced variability. The variations in emissivity might be attributed to changes in the chemical composition of the target or could even indicate the start of coalescence and sintering of the powder. Further characterization is still needed to confirm the occurrence of these effects, but it should be noted that this technique may provide a useful diagnostic method for identifying particle sintering and a variety of other useful PBF processing conditions, such as defect formation, that can be detected via accurate temperature and/or spectral emissivity measurements. The work described by Olinger et al. in [25] shows a diagram of the emissivity and temperature during solidification of a casting of a nickel superalloy, specifically showing the emissivity changes as a function of phase (i.e. liquid to solid transition). Similarly, in our work, as the material is

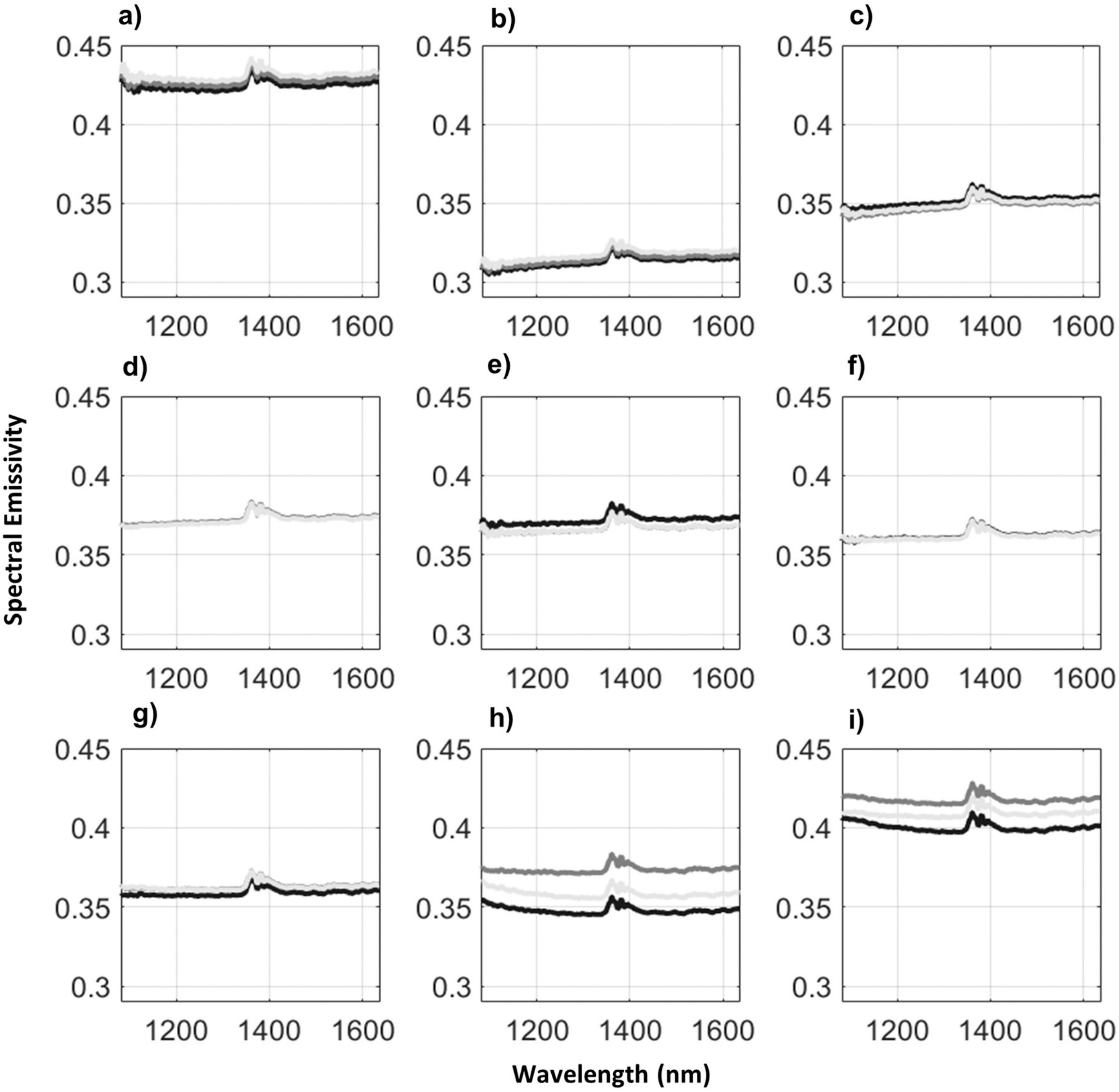

Fig. 7. Spectral emissivity plots for the nine preheating steps, corresponding to figure parts a) through i). The spectrums shown were calculated for the median temperature (gray), one minute before median temperature (light gray), and one minute after the median temperature (black).

being scanned by the electron beam during the preheating sequences, it is hypothesized that changes occur to the material, such as partial sintering, that change the morphology and perhaps chemistry of the sample, leading to abrupt changes in emissivity of the target, as exemplified in the varying plots in Fig. 7a)–i). The plots on emissivity in Fig. 7 show an anomaly at the wavelength range from ~1340 nm to ~1425 nm, represented as a double peak. This is a result of the calibration that was conducted in air (with humidity) before the experiments inside the Arcam A2 (in vacuum). This highlights environmental absorption effects due to the presence of humidity which might be an issue for single or two-color pyrometers that have a narrow waveband over this spectral range. The decrease in transmission provided by water vapor in the environment at that wavelength range is well described in [43,44]. The increase in radiation in the evacuated Arcam machine results in the double peaks for the emissivity plot over that wavelength range. Although the corrected intensity and the spectral target emissivity plots calculated by the instrument exhibit these peaks, this interference is discarded by the FMPI before the calculation of temperature [24]. The calibration of the FMPI in an inert gas environment can effectively remove this double peak feature.

3.3.2. *Melting steps*

Melting was induced in seven consecutive steps with no powder deposition and the time-dependent measured surface temperatures and emissivity values (at 1500 nm) are shown in Fig. 8a) and b), respectively. The emissivity values in the figure show quite remarkably the variation of emissivity throughout the melting, solidification, and cooling process, showing emissivity values of ~0.3 before the initial melt event (i.e., starting with the sintered powder after the pre-heating steps) and then varying between ~0.025 and ~0.15 during the subsequent melt events (melting, solidification, cooling). Fig. 8a) shows an almost mirrored behavior between the temperature and emissivity plots in which the minima values for emissivity (valleys) coincide with the maxima temperature values (peaks). Assuming the peak temperature corresponds with liquid phase (molten) copper and the minimum correspond with solidified copper, these emissivity values can be roughly compared with the published data of [45] for molten copper and [14] for solid copper. Prior to every melt event, a discontinuity is observed in the temperature and emissivity measured (as indicated by black arrows Fig. 8a)); this is a feature of the exposure time algorithm as described above. Also, the drop in emissivity shown in Fig. 8a) (indicated by gray arrows), is attributed to the rake mechanism moving

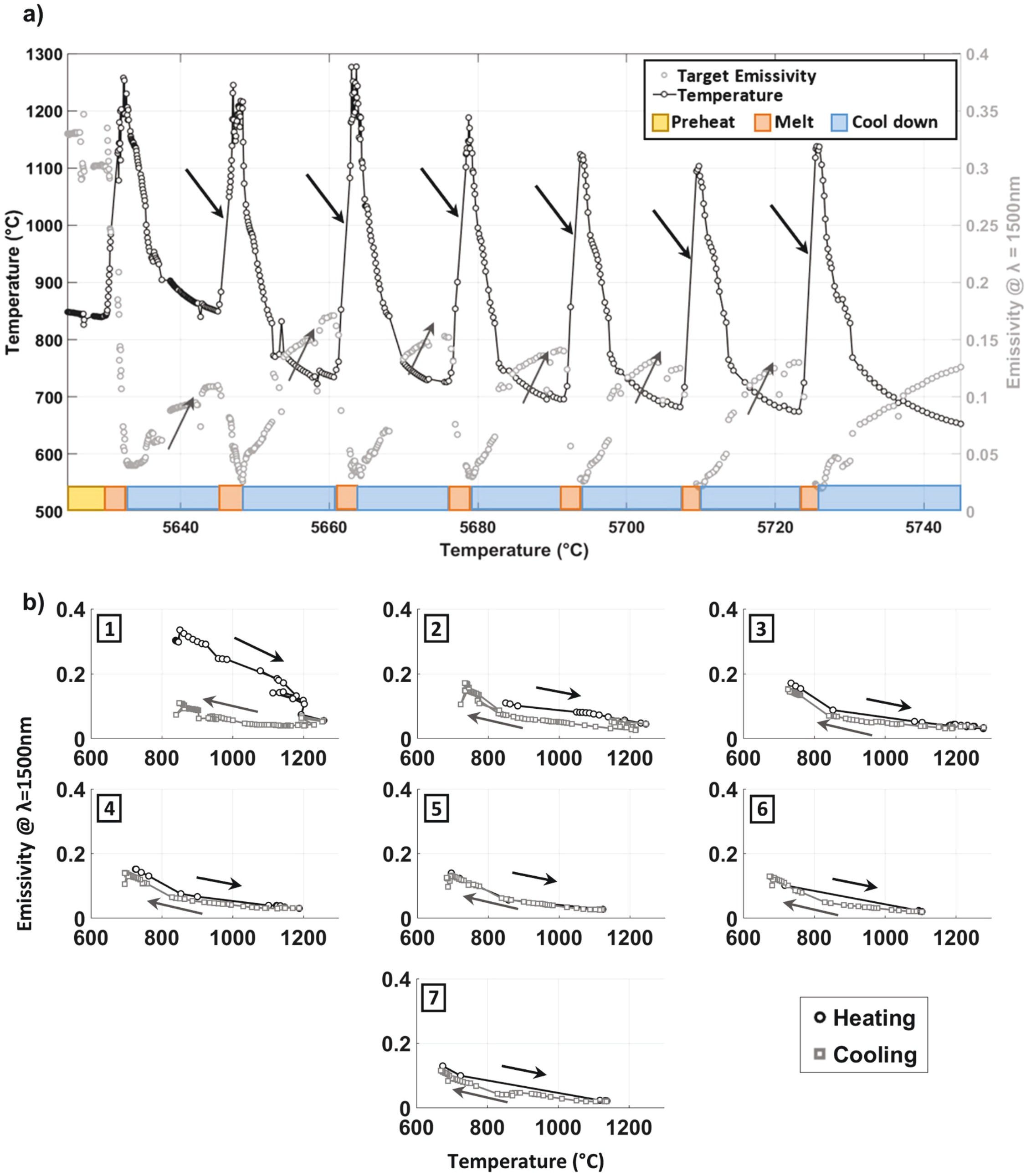

Fig. 8. a) Close up of temperature signals obtained by the FMPI during the seven melt steps. The plot includes a secondary axis of emissivity at 1500 nm obtained at those temperatures by the instrument. Temperature plot is depicted by the black line and the emissivity at 1500 nm plot is depicted by the gray line. b) Temperature against emissivity at 1500 nm plot for the seven melting steps indicated by boxed numbers; plots in black (unfilled circle markers) represent heating up until melt and the gray plots (unfilled square markers) represent the decrease in temperature upon cooling. Black and gray arrows are added to help visualize the heating and cooling trends. Colored boxes in Fig. 8a) are added to enhance reader's understanding of the heat transfer steps in the experiment.

across the measurement region and interfering with the measurements. Recall that no powder was wked during this process.

Fig. 8b) shows seven plots of emissivity (reported at λ = 1500 nm) vs temperature in which the heating up and cooling down stages for each melt are indicated in black and gray lines with unfilled markers, respectively. As seen in Fig. 8b) plot 1, the first melt event is indicated in the excursion for the values of emissivity starting at ~0.35 at a temperature of ~850 °C, followed by a progressive drop to ~0.05 at the highest temperature exceeding 1250 °C. The successive six melts (plots 2–7) are indicated during heating up (black lines with unfilled black circle markers) and cooling down (gray lines with unfilled square markers). The change in surface morphology that the material experiences as a result of the phase change (powder to liquid to solid) appears to coincide with the emissivity change. It should be noted that the emissivity values observed during the melting excursions shown in Fig. 8b) are consistent with observations reported in literature for phase change of copper [14]. The plots for the last six melts in Fig. 8b) indicate the emissivity makes excursions from below 0.05 during temperature peaks, to values approaching ~0.15 upon cooling down to ~700 °C. The emissivity values in the plot for the first melt in Fig. 8b) indicate the FMPI's ability to capture the phase transition as the copper powder undergoes melting and solidification. After this first melt event, there is agreement between the emissivities recorded for all subsequent melting excursions. This observation is supported by the fact that only the first melt excursion followed the powder-liquid-solid transition, whereas the subsequent steps essentially remelted a solid surface. Although

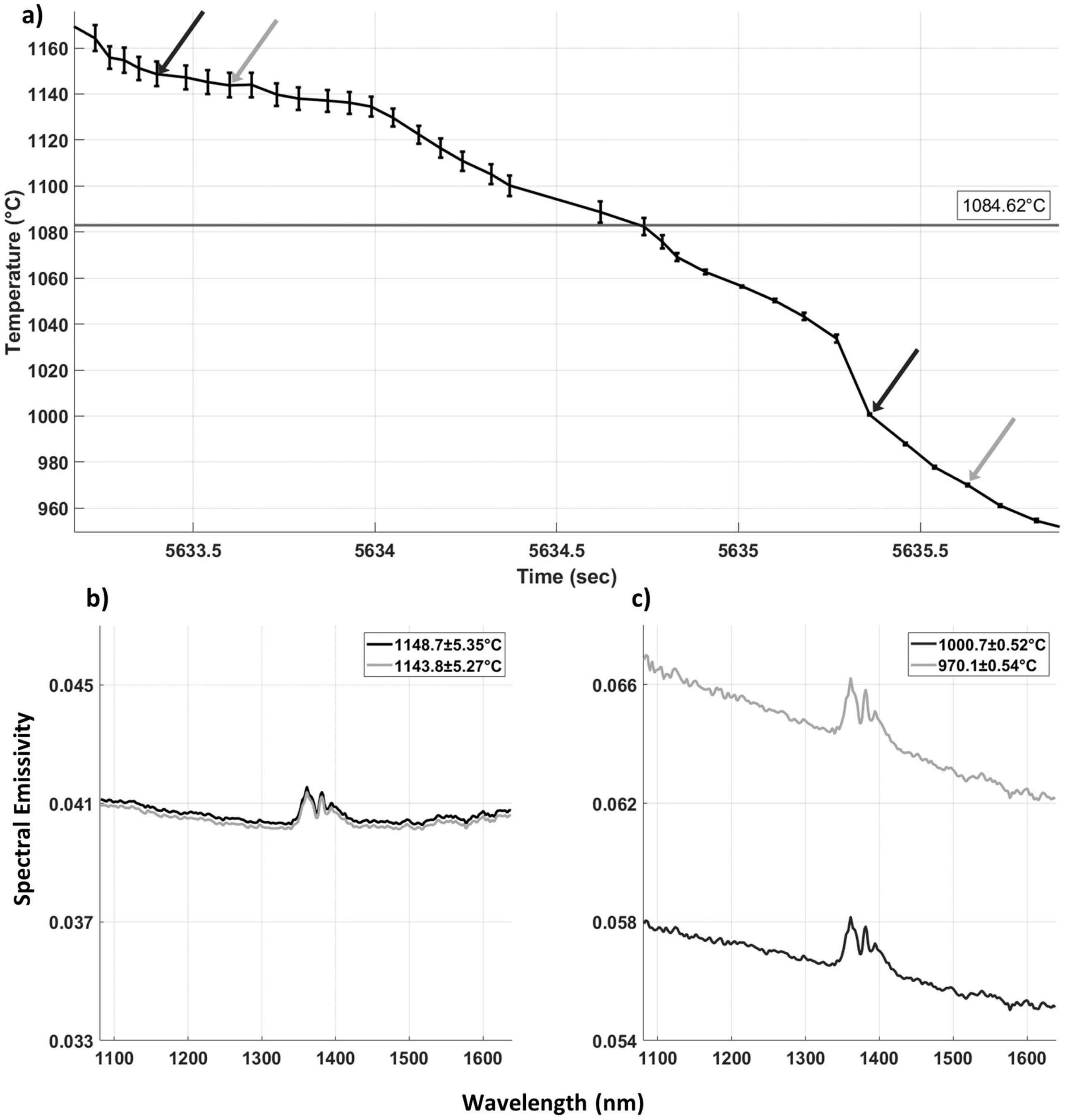

Fig. 9. a) Close up of decaying temperature for the first melt (i.e. after scanning) with standard deviation error bars. The arrows point at selected temperatures on the following plots. b) Spectral emissivity plots for selected temperatures above the melting temperature of copper. The black and gray line correspond to the black and gray arrows above the melting point of copper. c) Spectral emissivity plots for selected temperatures below the melting temperature of copper. The black and gray plots correspond to the black and gray arrows below the melting point of copper.

literature for copper powder is not available for comparison, the behavior showing the change in emissivity from the liquid (i.e. melt) to solid shown in our results (plots 2–7 in Fig. 8b)) show consistency, and are comparable to those reported in literature for liquid and solid copper [46].

Fig. 9a) shows the temperature decrease (i.e. cooling) following the first melt event, with error bars indicating the standard deviation as calculated by the FMPI pyrometer for each data point. The horizontal line in the figure indicates the melting point for copper (~1084 °C [47]), used to simply indicate a possible phase transition in the region of this temperature. The standard deviation above the melting point of copper is ~6 °C, and it drops to < 1 °C below the melting point. The difference in standard deviation is attributed to the FMPI pyrometer observing multiple coexisting phases (i.e. powder, liquid, and solidified copper) or a modest temperature gradient, or both. In the latter case, the relatively large size of the measurement spot compared to the melt pool can lead to higher standard deviation values. Below the melting point line, the low standard deviations in the measurements suggest the material has transitioned to the solid phase and is experiencing slower cooling conditions, compared with the rapid non-equilibrium solidification during melting.

The plots in Fig. 9b) and c) show the spectral emissivity for the temperatures, indicated by arrows (two above and two below the melting point) in Fig. 9a). For the two temperatures indicated above the melting point (i.e. ~1145 °C), emissivity exhibits a near graybody behavior, with a variation of ~2% (Fig. 9b)), within the 1080–1640 nm spectrum. However, the spectral emissivity variation (1080–1640 nm) is more drastic for the temperatures below the melting point resulting in ~7% difference, when comparing to the values at 1000.7 °C and 970.1 °C (Fig. 9c)). Fig. 9c) demonstrates the non-graybody behavior in addition to the well-known temperature dependence of emissivity for the copper material used in this study.

Existing literature in PBF AM is limited on the subject of the emissivity behavior of materials, such as the recent study by [48] for 316 L and Inconel 718. This study employed thermocouples to compare the temperatures acquired with a mid-wavelength infrared (MWIR) camera and allowed the calculation of apparent and corrected emissivity values, although emissivity was considered to exhibit graybody behavior in their analyses. However, to the authors’ knowledge, no study has directly addressed the non-graybody behavior of materials under representative processing conditions over a large spectral range, as presented in the current work. This is due, in part, to the current practice in the AM community to use radiation thermometry devices with limited spectral range capabilities, that are unable to capture the spectral response of targets, or those that rely on prior knowledge of the target’s emissivity including IR cameras, single-color, and two-wavelength pyrometers. Specifically, for two-wavelength pyrometers, the inability of such sensors to capture a more complete view of the spectral behavior of the materials during PBF processing could intrinsically limit accuracy of these devices. For example, a calculation using the ratio pyrometry equation [49] can be used to demonstrate some possible errors from using this approach to measure temperature for the experiment described here. Using the intensity values used to compute the emissivity captured in Fig. 9b) and c) at 1300 nm and 1550 nm (assuming these as the two discrete wavelengths of a two-wavelength pyrometer) would lead to only ~6–7 °C difference for the emissivity values in Fig. 9b) (graybody behavior) but up to ~27 °C difference at 970.1 °C in Fig. 9c) (non-graybody behavior). Although this 27 °C difference might be considered non-critical, it is instructive to mention that pure copper can be traditionally regarded as a spectrally well behaved (gray) material in the spectrum observed by [14], and hence differences in temperature readings from two wavelength radiation thermometers will not be as large. As an example of the greater difference that can be expected for other spectral ranges, an analysis can be done, using the error equation (Eq. (3)) as detailed in [22], for a two-color pyrometer (operating at the discrete wavelengths of 700 and 950 nm) which has been employed for monitoring in L-PBF by [40], and using the values of emissivity (non-gray by more than 50%) reported by [50]. The expected error for such an instrument at the melting point for copper (~1084 °C) can result in over 150 °C. An analysis of other two-color pyrometers working near the visible spectrum [51,52] would be expected to yield similar or even higher errors, as the emissive behavior of materials is more drastic in this range [14].

$$\Delta T = \frac{T^2}{C'} \frac{\lambda_2 \lambda_1}{(\lambda_2 - \lambda_1)} \frac{\Delta R}{R} \tag{3}$$

Different materials can also exhibit more pronounced non-graybody behavior including many alloys employed in PBF AM. The example with copper is intended to show the different dependencies of emissivity over the calibrated spectral range of the FMPI pyrometer, and also as a function of temperatures, phases, and processing conditions experienced in PBF. The knowledge of these dependencies is essential to better use and apply thermal signature measurement techniques commonly used in the PBF process. The authors are currently focusing on extending the current results to materials commonly used in PBF, such as Ti6Al4V, Inconel 718, and others.

4. Conclusion

This work has presented a novel method using a MW pyrometer for in situ acquisition of thermal signatures from a small region of a powder bed that was gradually heated up, in a total of nine steps, then melted in a series of seven successive melting steps, using electron beam scanning in a commercial EB-PBF Arcam A2 system. The method implemented a setup including a vacuum rated tube that enabled near continuous measurements using the MW pyrometer, and it also demonstrated the negligible effect of reflections from the radiative environment on the measurements obtained. The major contribution from this work is the overall method for measuring spectral emissivity of materials being processed in PBF with measurements performed during actual PBF processing (experiencing heating, sintering, melting, solidification, and cooling). The method was demonstrated on a copper powder for which the spectral (wavelength range from 1080 to 1640 nm) and temporal dependence of emissivity was measured. The spectral and temporal dependence for copper was captured while holding a near-constant temperature in each preheating step. This also indicates the temperature dependence of emissivity. All this behavior was captured in plots that showed that emissivity values ranged from ~0.30 to ~0.45 and exhibited a variability anywhere from 10% to 16%. The plots clearly indicated the non-graybody behavior of the material. Also, the emissivity change was measured across the phase change during melting and cooling of the material, indicating that emissivity was nearly constant (gray) above the melting point, but the material exhibited very non-gray behavior in the cooling region.

This complex behavior of emissivity found for copper, a feature that might also be observed for other metals processed using PBF AM, points to a major challenge in PBF AM in the application of non-contact temperature measurement methods for measuring accurate surface temperatures. These results highlighted some of the potential shortfalls in temperatures reported using non-contact radiation thermometry methods (such as two-color pyrometers and IR cameras) in current literature. For example, the work presented by [23] showed that a 15% error in near-IR emissivity (500 - 1000 nm) results in an observed temperature error of ± 100 °C during melting and cooling of a nickel superalloy. Further research will establish the full range of spectral response of emissivity for many other materials used in PBF. Additional research could include increasing the acquisition rate of the MW pyrometer and expanding the spectral range of its sensor. However, the setup and procedures described in this work can be immediately applied to other more commonly used materials to help establish their spectral emissivity during PBF processing, which is the current focus of ongoing work.

CRediT authorship statement contribution

Alfonso Fernandez: Data Interpretation, Analysis, Writing - review & editing, Writing - original draft, Experimentation, Data acquisition. **Ralph Felice**: Data interpretation, Writing - review & editing. **César A. Terrazas-Nájera**: Conceptualization, Experiment Design and Planning, Data Interpretation, Writing - review and editing, Writing - original draft. **Ryan Wicker**: Conceptualization, Supervision, Writing - review & editing, Funding acquisition.

Declaration of Competing Interest

One or more of the authors of this article are a part of the Editorial Board of the journal. To avoid a potential conflict of interest, the responsibility for the editorial and peer-review process of this article was handled by a different editor. Furthermore, the authors of this article were removed from the peer review process and had no, and will not have, any access to confidential information related to the editorial process of this article.

Acknowledgements

The research presented in this work was performed at the W.M. Keck Center for 3D Innovation (Keck Center), a state-of-the-art additive manufacturing research facility located within The University of Texas at El Paso (UTEP). The authors are grateful for support in various aspects of the research presented here provided by Keck Center faculty member Francisco Medina and students Sol Barraza, Sergio Estrada, and Kurtis Watanabe. Support for this research was directly provided by the Mr. and Mrs. MacIntosh Murchison Chair I in Engineering Endowment at UTEP (RBW), the LSAMP NSF HRD-1810898 grant, and through strategic investments in this research via discretionary funds from UTEP and the Keck Center.

References

[1] E. Rodriguez, J. Mireles, C.A. Terrazas, D. Espalin, M.A. Perez, R.B. Wicker, Approximation of absolute surface temperature measurements of powder bed fusion additive manufacturing technology using in situ infrared thermography, Addit. Manuf. 5 (2015) 31–39, https://doi.org/10.1016/j.addma.2014.12.001.

[2] J. Mireles, C. Terrazas, S.M. Gaytan, D.A. Roberson, R.B. Wicker, Closed-loop automatic feedback control in electron beam melting, Int. J. Adv. Manuf. Technol. (2014), https://doi.org/10.1007/s00170-014-6708-4.

[3] J. Schwerdtfeger, R.F. Singer, C. Körner, In situ flaw detection by IR-imaging during electron beam melting, Rapid Prototyp. J. 18 (2012) 259–263, https://doi.org/10.1108/13552541211231572.

[4] J. Mireles, S. Ridwan, P.A. Morton, A. Hinojos, R.B. Wicker, Analysis and correction of defects within parts fabricated using powder bed fusion technology, Surf. Topogr.: Metrol. Prop. 3 (2015), 034002, https://doi.org/10.1088/2051-672X/3/3/034002.

[5] R.B. Dinwiddie, M.M. Kirka, P.D. Lloyd, R.R. Dehoff, L.E. Lowe, G.S. Marlow, Calibrating IR cameras for in-situ temperature measurement during the electron beam melt processing of Inconel 718 and Ti-Al6-V4, Thermosense Therm. Infrared Appl. 9861 (2016), 986107, https://doi.org/10.1117/12.2229070.

[6] J. Raplee, A. Plotkowski, M.M. Kirka, R. Dinwiddie, A. Okello, R.R. Dehoff, S. S. Babu, Thermographic microstructure monitoring in electron beam additive manufacturing, Sci. Rep. 7 (2017) 1–16, https://doi.org/10.1038/srep43554.

[7] N. Boone, C. Zhu, C. Smith, I. Todd, J.R. Willmott, Thermal near infrared monitoring system for electron beam melting with emissivity tracking, Addit. Manuf. 22 (2018) 601–605, https://doi.org/10.1016/j.addma.2018.06.004.

[8] D.P. DeWitt, G.D. Nutter, Theory and Practice of Radiation Thermometry, John Wiley & Sons, Inc,, 1988.

[9] R.D. Murphy, E.C. Forrest, A Review of In-situ Temperature Measurements for Additive Manufacturing Technologies, in: 2016 NCSL Int. Work. Symp., St. Paul, MN, 2016.

[10] M. Vollmer, K.-P. Möllmann, Infrared Thermal Imaging, Wiley-VCH Verlag GmbH & Co. KGaA,, Weinheim, Germany, 2017, https://doi.org/10.1002/9783527693306.

[11] P.M. Cordero, J. Mireles, S. Ridwan, R.B. Wicker, Evaluation of monitoring methods for electron beam melting powder bed fusion additive manufacturing technology, Prog, Addit. Manuf. 2 (2017) 1–10, https://doi.org/10.1007/s40964-016-0015-6.

[12] J. Minjares, Fabrication Of A Nickel-Based Superalloy In Electron Beam Melting And Process Improvements Using Thermal Feedback From A Multi-Wavelength Pyrometer, University of Texas at El Paso, 2014.

[13] E.B. Curry, S. Sahoo, C. Herrera, I. Sochnikov, S. Pamir Alpay, R.J. Hebert, B. G. Willis, J. Qi, J.N. Hancock, Optical response of nickel-based superalloy Inconel-718 for applications in additive manufacturing, J. Appl. Phys. 127 (2020), 245111, https://doi.org/10.1063/5.0006006.

[14] Y.S. Tolukian, D.P. DeWitt, Thermal Radiative Properties - Metallic Elements and alloys, in: Thermophys. Prop. MATTER, 1970.

[15] T. Ishikawa, C. Koyama, Y. Nakata, Y. Watanabe, P.F. Paradis, Spectral emissivity and constant pressure heat capacity of liquid titanium measured by an electrostatic levitator, J. Chem. Thermodyn. 131 (2019) 557–562, https://doi.org/10.1016/j.jct.2018.12.002.

[16] L. González-Fernández, E. Risueño, R.B. Pérez-Sáez, M.J. Tello, Infrared normal spectral emissivity of Ti-6Al-4V alloy in the 500–1150 K temperature range, J. Alloy. Compd. 541 (2012) 144–149, https://doi.org/10.1016/j.jallcom.2012.06.117.

[17] Omega, ANSI and IEC color codes for thermocouples, wire and connectors, n.d. https://assets.omega.com/pdf/test-and-measurement-equipment/temperature/sensors/thermocouple-probes/tc_colorcodes.pdf (Accessed 15 April 2021).

[18] Q. Guo, C. Zhao, L.I. Escano, Z. Young, L. Xiong, K. Fezzaa, W. Everhart, B. Brown, T. Sun, L. Chen, Transient dynamics of powder spattering in laser powder bed fusion additive manufacturing process revealed by in-situ high-speed high-energy x-ray imaging, Acta Mater. 151 (2018) 169–180, https://doi.org/10.1016/j.actamat.2018.03.036.

[19] M.A. Lodes, R. Guschlbauer, C. Körner, Process development for the manufacturing of 99.94% pure copper via selective electron beam melting, Mater. Lett. 143 (2015) 298–301, https://doi.org/10.1016/j.matlet.2014.12.105.

[20] Metal powder in copper alloys — Metal powder | Sandvik, (n.d.). https://www.metalpowder.sandvik/en/products/metal-powder-alloys/copper-alloys/ (Accessed 15 April 2021).

[21] R.A. Felice, The Spectropyrometer – a Practical Multi-wavelength Pyrometer, in: 8th Symp. Temp. Its Meas. Control Sci. Ind., 2002.

[22] R.A. Felice, Temperature Determining Device And Process, US 6,379,038 B1, 2002.

[23] R.A. Felice, Investment Casting Temperature Measurement, Foundry Manag. Technol, 2006.

[24] R.A. Felice, Multispectral expert system spectropyrometer and its uses in industry and research, Thermosense XXVI 5405 (2004) 36, https://doi.org/10.1117/12.547800.

[25] D.M. Olinger, R.A. Felice, J. V. Gray, Successful Pyrometry in Investment Casting, Invest. Cast. Inst. 55th Tech. Conf. Expo. (2007).

[26] R. Felice, D. Nash, Pyrometry of materials with changing, spectrally-dependent emissivity - Solid and liquid metals, AIP Conf Proc 1552 (8) (2013) 734–739, https://doi.org/10.1063/1.4819633.

[27] D. Riedlbauer, T. Scharowsky, R.F. Singer, P. Steinmann, C. Körner, J. Mergheim, Macroscopic simulation and experimental measurement of melt pool characteristics in selective electron beam melting of Ti-6Al-4V, Int. J. Adv. Manuf. Technol. 88 (2017) 1309–1317, https://doi.org/10.1007/s00170-016-8819-6.

[28] G. Ruffino, Two-colour pyrometry on nonisothermal fields: a measurement problem in siderurgy, High. Temp. - High. Press 6 (1974) 223–227.

[29] C.G. Ren, Y.L. Lo, H.C. Tran, M.H. Lee, Emissivity calibration method for pyrometer measurement of melting pool temperature in selective laser melting of stainless steel 316L, Int. J. Adv. Manuf. Technol. 105 (2019) 637–649, https://doi.org/10.1007/s00170-019-04193-0.

[30] Thermocouple Response Time | Omega Engineering, Omega Eng. 2003. https://www.omega.com/en-us/resources/thermocouples-response-time (Accessed 17 September 2020).

[31] D.J. Dagel, G.D. Grossetete, D.O. MacCallum, S.P. Korey, Four-color imaging pyrometer for mapping temperatures of laser-based metal processes, in: J. N. Zalameda, P. Bison (Eds.), Thermosense Therm. Infrared Appl. XXXVIII, SPIE, 2016, https://doi.org/10.1117/12.2223083.

[32] M. Doubenskaia, P. Bertrand, I. Smurov, Optical monitoring of Nd:YAG laser cladding, Thin Solid Films 453–454 (2004) 477–485, https://doi.org/10.1016/j.tsf.2003.11.184.

[33] I. Smurov, M. Doubenskaia, Temperature Monitoring by Optical Methods in Laser Processing. Laser-Assisted Fabrication of Materials, Springer, Berlin, Heidelberg, 2013, pp. 375–422, https://doi.org/10.1007/978-3-642-28359-8_9.

[34] Y. Chivel, I. Smurov, On-line temperature monitoring in selective laser sintering/melting, in: Phys. Procedia, Elsevier B.V, 2010, pp. 515–521, https://doi.org/10.1016/j.phpro.2010.08.079.

[35] Y. Chivel, I. Smurov, Temperature monitoring in selective laser sintering/melting, Fundam. Laser-Assist. Micro- Nanotechnol. 2010 (7996) (2010) 79960A, https://doi.org/10.1117/12.887310.

[36] Y. Chivel, I. Smurov, Temperature monitoring and overhang layers problem, in: Phys. Procedia, Elsevier B.V, 2011, pp. 691–696, https://doi.org/10.1016/j.phpro.2011.03.086.

[37] J.M. Montgomery, M.J. Lipp, Z. Jenei, Y. Meng, W.J. Evans, A simple and portable multi-channel pyrometer allowing temperature measurements down to 800 K on the microsecond scale, Rev. Sci. Instrum. 89 (2018), 125117, https://doi.org/10.1063/1.5048784.

[38] R. Wang, S. Li, W. Zhou, Z.X. Luo, J. Meng, J. Tian, L. He, X. Cheng, A high-speed, eight-wavelength visible light-infrared pyrometer for shock physics experiments, AIP Adv. 7 (2017), 095014, https://doi.org/10.1063/1.4996927.

[39] K. Bala, P.R. Pradhan, N.S. Saxena, M.P. Saksena, Effective thermal conductivity of copper powders, J. Phys. D. Appl. Phys. 22 (1989) 1068–1072, https://doi.org/10.1088/0022-3727/22/8/009.

[40] U. Scipioni Bertoli, G. Guss, S. Wu, M.J. Matthews, J.M. Schoenung, In-situ characterization of laser-powder interaction and cooling rates through high-speed imaging of powder bed fusion additive manufacturing, Mater. Des. 135 (2017) 385–396, https://doi.org/10.1016/j.matdes.2017.09.044.

[41] P.A. Hooper, Melt pool temperature and cooling rates in laser powder bed fusion, Addit. Manuf. 22 (2018) 548–559, https://doi.org/10.1016/j.addma.2018.05.032.

[42] C. Zhao, K. Fezzaa, R.W. Cunningham, H. Wen, F. De Carlo, L. Chen, A.D. Rollett, T. Sun, Real-time monitoring of laser powder bed fusion process using high-speed X-ray imaging and diffraction, Sci. Rep. 7 (2017) 1–11, https://doi.org/10.1038/s41598-017-03761-2.

[43] F.E. Fowle, The transparency of aqueous vapor, ApJ 42 (1915) 394, https://doi.org/10.1086/142220.

[44] The Sites | Gemini Observatory, (n.d.). https://www.gemini.edu/observing/telescopes-and-sites/sites#0.9–2.7um (Accessed 12 October 2020).

[45] R. Kurosawa, T. Inoue, Y. Baba, K.I. Sugioka, M. Kubo, T. Tsukada, H. Fukuyama, Normal spectral emissivity measurement of molten copper using an electromagnetic levitator superimposed with a static magnetic field, Meas. Sci. Technol. 24 (2013), 015603, https://doi.org/10.1088/0957-0233/24/1/015603.

[46] C. Cagran, G. Pottlacher, Normal spectral emissivities of liquid copper, liquid gold and liquid silver at 684.5 nm, J. Non Cryst. Solids 353 (2007) 3582–3586, https://doi.org/10.1016/j.jnoncrysol.2007.05.117.

[47] H. Preston-Thomas, The international temperature scale of 1990 (ITS-90), Metrologia 27 (1990) 3–10.

[48] G. Mohr, S. Nowakowski, S.J. Altenburg, C. Maierhofer, K. Hilgenberg, TASCI-transcutaneous tibial nerve stimulation in patients with acute spinal cord injury to prevent neurogenic detrusor overactivity: protocol for a nationwide, randomised, sham-controlled, double-blind clinical trial, BMJ Open 10 (2020), 039164, https://doi.org/10.3390/met10111546.

[49] D. Ketui, F. Chi, G. Shan, Single wavelength and ratio pyrometry reflection errors in temperature measurement of gas turbine blade, Measurement 86 (2016) 133–140, https://doi.org/10.1016/j.measurement.2016.02.054.

[50] H. Watanabe, M. Susa, H. Fukuyama, K. Nagata, Phase dependence (Liquid/Solid) of normal spectral emissivities of noble metals at melting points, Int. J. Thermophys. 24 (2003) 223–237, https://doi.org/10.1023/A:1022374501754.

[51] M. Mahmoudi, A.A. Ezzat, A. Elwany, Layerwise anomaly detection in laser powder-bed fusion metal additive manufacturing, J. Manuf. Sci. Eng. Trans. ASME 141 (2019), https://doi.org/10.1115/1.4042108.

[52] J.A. Mitchell, T.A. Ivanoff, D. Dagel, J.D. Madison, B. Jared, Linking pyrometry to porosity in additively manufactured metals, Addit. Manuf. 31 (2020), 100946, https://doi.org/10.1016/j.addma.2019.100946.